



# Sunlight-driven photocatalytic degradation of methylene blue using ZnO/biochar nanocomposite derived from banana peels

Prabakaran Eswaran<sup>1</sup> · Priya Dharshini Madasamy<sup>2</sup> · Kriveshini Pillay<sup>3</sup> · Hendrik Brink<sup>1</sup>

Received: 9 May 2024 / Revised: 24 July 2024 / Accepted: 25 July 2024  
© The Author(s) 2024

## Abstract

This study describes the preparation of zinc oxide nanocomposite and its application as photocatalyst in the degradation of methylene blue under sunlight irradiation. Zinc oxide-coated biochar (ZnO/BC) nanocomposite was prepared using the hydrothermal method from banana peels and zinc acetate dihydrate as precursors. The biochar (BC), ZnO nanoparticles (ZnONPs), and ZnO/BC nanocomposite were characterized, and the results showed that ZnONPs had definite crystallinity and a regular surface morphology, with particles approximately 18 nm in size, and a XRD pattern corresponding to ZnONPs. In contrast, the ZnO/BC nanocomposite exhibited a more amorphous structure consistent with wurtzite (ZnO) and an irregular surface morphology with clusters of white particles measuring around 20–30 nm. Tauc's plot was used to calculate the band gaps energy of ZnONPs (3.04 eV) and ZnO/BC nanocomposite (2.89 eV). Catalyst-free, ZnONPs, and ZnO/BC nanocomposite were utilized for the photocatalytic degradation of methylene blue (MB) under sunlight irradiation for 0 to 120 min in which ZnO/BC nanocomposite showed excellent photocatalytic degradation of MB under sunlight irradiation at 0 to 120 min due to lower band gap energy and synergetic effect between ZnO and BC. Dosages of 100 mg (ZnO/BC nanocomposite) and 10 ppm (MB) were optimized to obtain the best photocatalytic degradation efficiency (92 %) under sunlight irradiation with 0 to 120 min. The process was conducted with various parameters like dosage variation, concentration of MB, and different pH 3, 5, 8, and 10 to improve the photocatalytic degradation of MB from wastewater. The results indicated that the optimal conditions for the photocatalytic degradation of MB (92% after 120 min) were a catalyst dosage of 100 mg, an MB concentration of 10 ppm, and a pH of 10. This work demonstrates the potential of ZnO/BC nanocomposite photocatalyst for application in wastewater treatment and environment remediation.

**Keywords** Banana peel · ZnO/biochar nanocomposite · Methylene blue · Photocatalytic activity · Sunlight irradiation

## 1 Introduction

Water pollution stands as a significant global concern, exerting far-reaching impacts on both climate and the environment, affecting various life forms [1]. Bodies of water worldwide have been compromised due to the influx of dyes

from industrial processes, especially the textile sector, with MB dye among the pollutants posing a particular threat to freshwater resources [2]. Given the escalating demand, the production of dyes is slated to rise, necessitating diverse techniques such as biological, chemical, pharmaceutical, pulp, dye processing, and waste management to address the issue [3]. Traditional methods like adsorption on activated carbon, reverse osmosis, ultra-filtration, coagulation by chemical agents, and ion exchange on synthetic adsorbent resins are being replaced by novel approaches.

Methylene blue (MB) dye has found widespread use across industries like paper, paint, textiles, pharmaceuticals, cosmetics, and food [4, 5]. Regrettably, the wastewater from these sectors, when combined with drinking water, results in heavily contaminated water harboring dangerous pollutants for both humans and animals [6]. Exposure to MB triggers severe health problems, including nausea, mental confusion,

✉ Hendrik Brink  
deon.brink@up.ac.za

<sup>1</sup> Department of Chemical Engineering, Water Utilization and Environmental Engineering Division, University of Pretoria, Pretoria, South Africa

<sup>2</sup> PG & Research Department of Chemistry, Sri Paramakalyani College, Alwarkurichi 627 412, TamilNadu, India

<sup>3</sup> Department of Chemical Sciences, University of Johannesburg, Doornfontein Campus, Johannesburg 2028, South Africa

vomiting, methemoglobinemia, eye irritation, and profuse sweating [2]. An array of techniques has been explored to eliminate MB from water, ranging from filtration, adsorption, and electrochemical oxidation to reverse osmosis, membrane separation, ion exchange, and catalytic reactions [7–14]. Nonetheless, these techniques have their limitations, including high costs, protracted procedures, and incomplete MB removal. Considering their affordability, ease of use, photocatalytic reaction, and post-mineralization catalyst retrieval, photocatalytic methods have emerged as a viable solution [15, 16].

In recent years, advanced oxidation processes (AOPs) have gained traction as swift, efficient, and non-toxic approaches, with the photo-Fenton reaction, ozonation, and photocatalysis playing pivotal roles in degrading various pollutants, both organic and inorganic [17–19]. Photocatalytic degradation serves diverse purposes, spanning wastewater treatment, air purification, sterilization, heavy metal remediation, and pollution breakdown [20]. While activated carbon is a mainstay in wastewater treatment, its high production costs necessitate alternate activation methods [21]. Biomass conversion methods like pyrolysis, combustion, liquefaction, gasification, and others have been explored as cost-effective activation strategies [22–24]. There has been a recent emphasis on semiconductor photocatalysts as effective instruments for environmentally friendly wastewater treatment, operating on the principle of decomposing pollutants into benign byproducts [25, 26]. Various semiconducting metal oxides, such as  $\text{TiO}_2$ ,  $\text{CeO}_2$ ,  $\text{ZnO}$ ,  $\text{SnO}_2$ , and  $\text{CuO}$ , have undergone thorough investigation as photocatalysts [27–31].  $\text{ZnO}$ , due to its cost-effectiveness, chemical stability, and efficacy, has garnered significant attention [32, 33]. Photocatalysis offers advantages such as the utilization of clean solar energy, high efficiency, and minimal generation of hazardous waste, making it applicable in diverse fields, ranging from environmental remediation to materials science [34]. Key characteristics of photocatalysts include their extensive active surface area, effective charge separation, ability to absorb visible light, and enduring photostability. Despite the preference for  $\text{ZnO}$  nanoparticles in photocatalytic applications over bulk materials, they exhibit certain limitations, such as solubility in acidic conditions, photo-leaching in basic solutions under UV light, rapid electron-hole recombination, and insufficient absorption of visible light energy [35].

Over the last decade, biochar has been produced through thermal means from diverse biomass sources like plant waste, wood chips, banana peels, orange peels, and coconut shells [36, 37]. Biochar boasts distinct physicochemical attributes like a generous surface area, strong carbonaceous properties, and superior electrical conductivity [38]. Its exceptional adsorption capacity aids in full mineralization of organic pollutants, while also curtailing electron-hole

recombination during photocatalytic degradation. Moreover, biochar is environmentally friendly, renewable, and cost-effective [39]. Bananas, rich in fibers, vitamins B6 and C, potassium, and magnesium, confer numerous health benefits like aiding digestion and weight management [40]. Banana peels are replete with oxygen, hydrogen, and carbon, forming functional groups like carboxylic and hydroxyl groups on the biochar surface, proving instrumental in organic dye and pesticide degradation [41].

Various metal oxide-coated biochar nanocomposites, like carboxymethyl cellulose-modified  $\text{ZnO}$ -biochar nanocomposite,  $\text{ZnO}$ -encapsulated biochar nanocomposite using cotton stalks, and  $\text{ZnO}$ -betaine-modified biochar nanocomposites, have been prepared using different biomass sources [42–44].  $\text{ZnO}$ -coated biochar nanocomposites bring the advantages of increased surface area, heightened reactive sites, improved dispersion, robust electron transfer between  $\text{ZnO}$  and biochar, and amplified photocatalytic activity [45, 46]. Recent advancements have led to porous carbon-supported  $\text{ZnO}$  nanocomposites, expanding raw materials and enhancing photocatalytic performance [47]. While the full scope of  $\text{ZnO}$ /biochar nanocomposite's potential remains untapped, its microstructure has shown promise in augmenting photocatalytic degradation through biochar supplementation [48]. Hence, the fusion of  $\text{ZnO}$  nanoparticles and biochar holds substantial promise in the photocatalytic degradation of organic pollutants, with the  $\text{ZnO}$ /biochar nanocomposite demonstrating significant potential for photodegradation studies.

There is currently significant interest in the potential applications of biochar produced through the pyrolysis of biomass. These biochars are made from inexpensive, environmentally friendly, renewable natural resources and involve simple techniques for creating functionalized carbon-based materials [49]. The creation of biochar and  $\text{ZnO}$  nanocomposites offers several advantages, such as increased adsorption capacity, high surface area, numerous active sites, well-established structures, and improved dispersion of  $\text{ZnO}$  nanoparticles on the biochar surface [50, 51]. The nanocomposite catalyst developed enhances photocatalytic degradation efficiency [52]. Notably, Leichtweis et al. discovered that the interaction between  $\text{Cu/Fe}_2\text{O}_4$  and biochar enhanced the photocatalytic degradation activity of the  $\text{CuFe}_2\text{O}_4$ /biochar nanocomposite. This interaction also improved charge carrier separation, adsorption capacity, and electron transfer mediation [53]. Meena et al. developed a green biochar-supported  $\text{ZnFe}_2\text{O}_4$  composite photocatalyst that effectively degrades MB under visible light irradiation [54]. Additionally, pomegranate peels were used to create a  $\text{ZnO}$  composite supported by biochar, enhancing the photocatalytic activity of  $\text{ZnO}$  nanoparticles. The biochar-encapsulated  $\text{ZnO}$  nanocomposite, with its multiple active sites, supports increased adsorption of organic pollutants

and generates highly reactive radicals, thus boosting visible light absorption and photocatalytic efficiency [55, 56]. Sun et al. reported that a hybrid nanocomposite photocatalyst based on g-C<sub>3</sub>N<sub>4</sub>/ferrite and biochar demonstrated excellent photocatalytic degradation of dyes and enhanced adsorption of organic pollutants, making it suitable for wastewater treatment systems [57].

To date, no known reports have focused on the work presented in this study. In this investigation, a ZnO/BC nanocomposite was synthesized using the hydrothermal method, utilizing banana peels to produce biochar. The biochar was then modified with ZnO to form the nanocomposite. Characterization of the materials was conducted using techniques such as FT-IR, UV-visible spectroscopy, XRD, SEM, and TEM. The design of the ZnO/BC nanocomposite aimed to enhance light absorption, alleviate photogenerated electron-hole recombination, and fortify photocatalytic capabilities. The experimental evaluation of the materials focused on their photocatalytic degradation of methylene blue (MB) under sunlight irradiation, comparing the photocatalytic efficiency of ZnO with that of the ZnO/BC nanocomposite. As a result, the ZnO/BC nanocomposite emerged as a crucial agent in advancing our understanding of the photocatalytic process and the catalytic mechanisms involved.

## 2 Experimental section

### 2.1 Chemicals and reagents

Banana peels were collected from a nearby market in Tenkasi, India (*circa* N8.96°, E77.31°). Analytical-grade Zinc acetate dihydrate (Zn(OAc)<sub>2</sub>·2H<sub>2</sub>O) and methylene blue (MB) were procured from Sigma-Aldrich, India. Sodium hydroxide (NaOH), hydrochloric acid (HCl), and ethanol were sourced from Sisco Research Laboratories (SRL) PVT Ltd., India ([www.vijayascientific.com](http://www.vijayascientific.com)). Distilled water was employed for all experimental procedures.

### 2.2 Preparation of ZnO nanoparticles

A 0.1M solution of Zn(OAc)<sub>2</sub>·2H<sub>2</sub>O was prepared by dissolving 2.0 g of the salt in 80 mL of distilled water and stirring for 30 min. Subsequently, a 2.5 M solution of NaOH was obtained by mixing 1.0 g of NaOH with 10 mL of distilled water stirring for 20 min. This NaOH solution was then gradually added to the Zn(OAc)<sub>2</sub>·2H<sub>2</sub>O solution while stirring, resulting in a white precipitate. The mixture was stirred for an additional hour to ensure proper formation of the precipitate.

The resulting solution, now containing the white precipitate, was transferred into a 100-mL Teflon-coated autoclave. This autoclave was placed in a muffle furnace and

maintained at a temperature of 180 °C for duration of 12 h. After this thermal treatment, the precipitate was recovered by centrifugation. This centrifugation process was repeated five times, alternating between distilled water and ethanol as the washing agents. The autoclave was allowed to cool to room temperature before starting the washing procedure. To obtain powdered ZnO nanoparticles, the white precipitate was subjected to a final drying step. This involved drying the precipitate at a temperature of 400 °C for duration of 2 h.

### 2.3 Synthesis of ZnO/BC nanocomposite

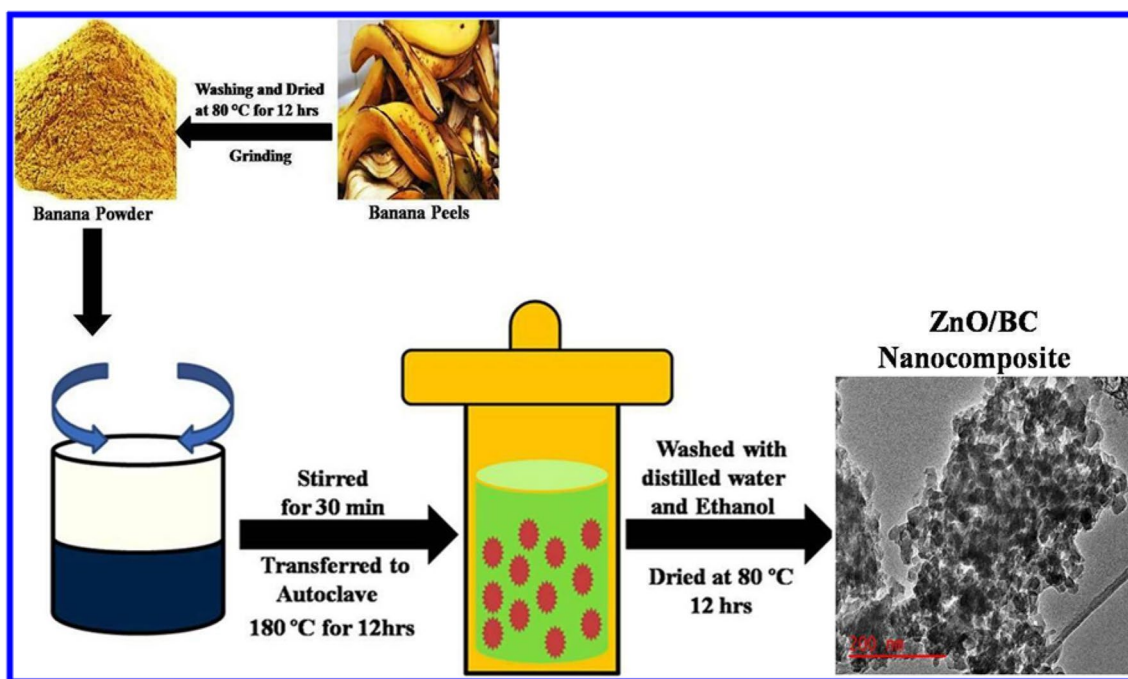
The collected banana peels underwent a thorough cleansing process, involving two rounds of washing with water to eliminate any impurities. Following this, they were allowed to naturally dry for 4 days under sunlight. Subsequently, the dried peels were finely ground into powder form. This powder served as a foundational material for crafting a nanocomposite featuring biochar-coated zinc oxide, referred to as ZnO/BC.

To create the nanocomposite, a 250-mL beaker was employed, wherein 4.0 g of banana peel powder and 2.0 g of zinc acetate dihydrate were combined. To this mixture, 80 mL of distilled water was introduced. The mixture was homogenized by stirring the solution using a magnetic stirrer for duration of 30 min. The next step involved transferring the solution into a 100-mL Teflon-coated autoclave, which was then positioned within a muffle furnace set at 180°C for a period of 6 h.

Upon completing the autoclave treatment, the resulting precipitate was gathered through centrifugation at a speed of 5000 rpm for 10 min. Subsequently, the precipitate was cleaned using multiple washes with a combination of water and ethanol to ensure the removal of any residual components. The washed precipitate was then meticulously collected and subjected to drying within an oven maintained at 80 °C for a span of 12 h. This meticulous process culminated in the production of a distinctive black powder. The visual representation of the entire procedure is illustrated in the accompanying Scheme 1.

### 2.4 Characterization methods

The present study employed a range of characterization techniques for the assessment of materials. The ZnONP and ZnO/BC nanocomposite powder samples were suspended in distilled water prior to measuring the optical properties using a UV-visible spectrometer (Double beam, Model: UH-5300, HITACHI). Functional group analysis of the materials was conducted with Fourier transform infrared (FT-IR) spectroscopy using an ID7ATR Thermo Scientific/NicoLET IS5 instrument.



**Scheme 1** Schematic diagram of the synthesis of ZnO/BC nanocomposite by using hydrothermal method

Fluorescence behavior of ZnONPs and the ZnO/BC nanocomposite was examined with a fluorescence spectrometer (Perkin Elmer). Crystalline properties were assessed using an X-ray diffractometer (Philips PW1729), with Cu K $\alpha$  radiation ( $\lambda = 1.5406 \text{ \AA}$ ) and operating at 45 kV and 40 mA.

Surface morphology and elemental composition analysis were performed using scanning electron microscopy (SEM) with a Carl Zeiss model (Ultra Plus). Size determination of ZnONPs and the ZnO/BC nanocomposite was achieved with transmission electron microscopy (TEM) using a JEOL JEM-2100F instrument, operating at an electron accelerating voltage of 200 kV.

## 2.5 Photocatalytic degradation method

The investigation into the photocatalytic activity of ZnO nanoparticles (ZnONPs) and the ZnO/biochar (ZnO/BC) nanocomposite for MB dye degradation was carried out through a series of photocatalytic studies. To initiate the experimentation, a stock solution of 0.05 g of MB dye, equivalent to 100 parts per million (100 ppm), was dissolved in distilled water within a standard 1L measuring flask. Subsequently, a quantity of 10 mL from this stock solution, constituting 10 ppm of MB dye, was added to a 100-mL standard measuring flask, wherein it was reconstituted with distilled water. This solution, having the desired concentration, was utilized for the ensuing experiments.

The photocatalytic degradation reactions were executed by introducing 100 mg of the photocatalysts into a 100 mL

solution of 10 ppm MB dye within a glass beaker. To ensure a well-dispersed mixture and attain an adsorption/desorption equilibrium, the amalgam was stirred in the dark for duration of 30 min. Following this, the suspension was subjected to natural sunlight irradiation. At specific intervals of time, 10 mL of the solution was extracted and subjected to filtration using a 0.45- $\mu\text{m}$  syringe filter to eliminate the presence of photocatalysts.

The collected solution underwent assessment for MB dye concentration using a UV-Vis spectrophotometer. Specifically, the absorbance at 664 nm was examined during the degradation process. This procedure allowed for the continuous monitoring and evaluation of the degradation process over different time intervals of 20 min. The percentage of MB degradation efficiency (%) was calculated using the following equation (1) [58, 59]:

$$\text{Degradation efficiency } \eta (\%) = C_0 - C_t \times 100 / C_0 \quad (1)$$

where  $C_0$  and  $C_t$  represent the absorbance of MB solution before and after the photocatalytic degradation activity. The said procedure was also used for the dosages, concentrations of MB, pHs, stability, and scavenger studies. The pHs were adjusted by using 0.1 M HCl or 0.1 M NaOH. Degradation kinetic rate constants of MB with ZnONPs and ZnO/BC nanocomposite were evaluated by using the first-order rate equation as given below [60]:

$$\ln C_t / C_0 = -kt \quad (2)$$

where  $C_0$  is the initial concentration and  $C_t$  is the final concentration before and after irradiation time  $t$ .  $k$  is the degradation rate constant ( $\text{min}^{-1}$ ).

## 2.6 Scavenger trapping methods

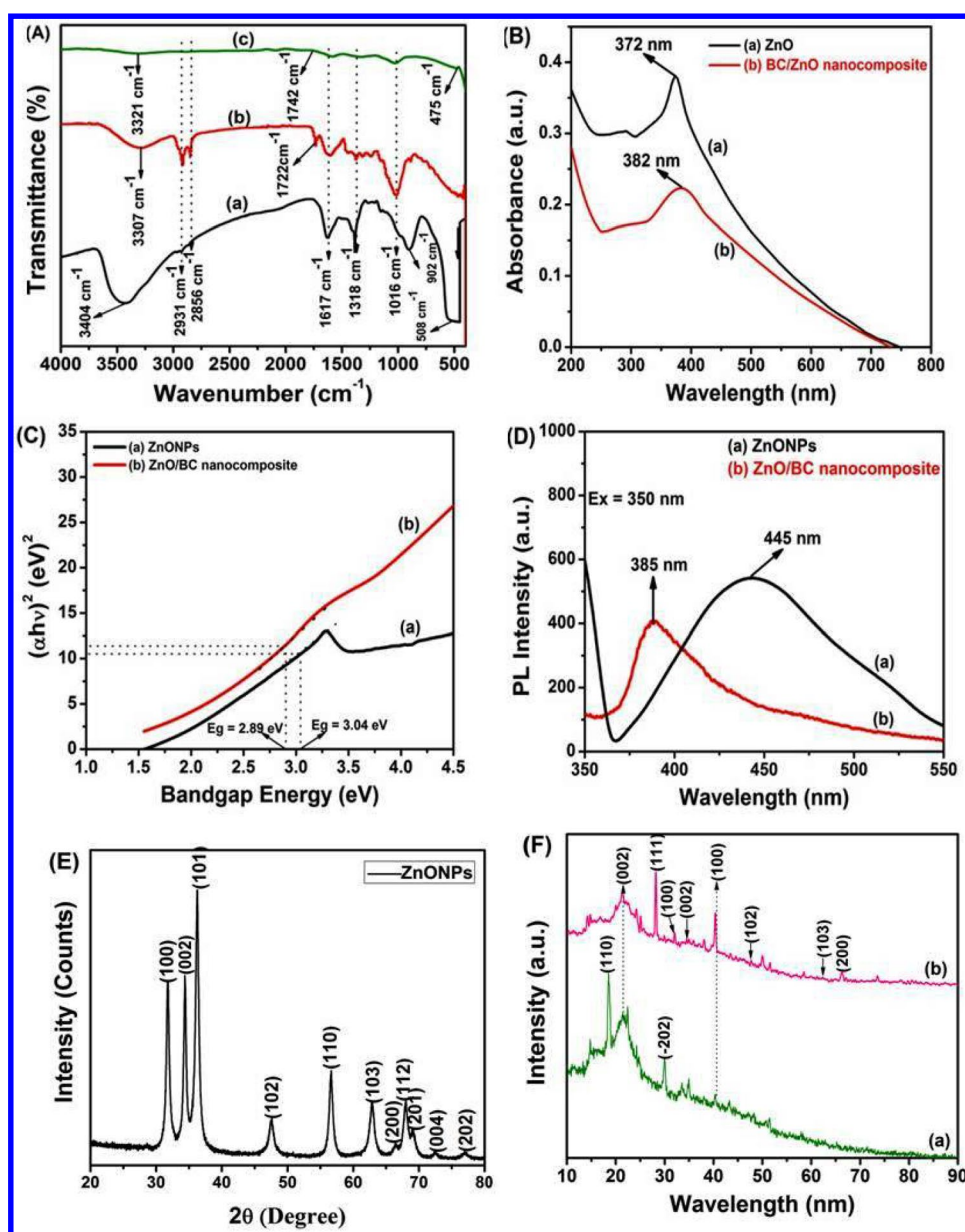
Scavenger trapping methods were used to determine the active species during the photocatalytic degradation of MB under sunlight irradiation. Isopropanol (IPA), phosphoric acid ( $\text{H}_3\text{PO}_4$ ), ethylenediaminetetraacetic acid (EDTA), and sodium persulfate ( $\text{Na}_2\text{S}_2\text{O}_8$ ) were used as scavengers for quench  $\cdot\text{OH}$ ,  $\cdot\text{O}_2^-$ ,  $\text{h}^+$ , and  $\text{e}^-$ , respectively. This method was conducted during the photocatalytic degradation of MB by 0.1 M scavengers.

## 3 Result and discussion

### 3.1 FT-IR characterizations

FT-IR spectra are used to evaluate the organic functional groups, metal-oxygen vibration bands, and changes in metal-oxygen frequency due to modification. The FT-IR spectra of ZnONPs, BPs, and ZnO/BC nanocomposite are displayed in Fig. 1A (a–c). A broad absorption peak at  $3404\text{ cm}^{-1}$  is associated with the O-H stretching vibration band of hydration on the ZnO surface [61, 62]. A double peak at  $2931\text{ cm}^{-1}$  and  $2856\text{ cm}^{-1}$  is attributed to the  $=\text{CH}_2$  and C-H bands stretching vibration from the

**Fig. 1** A–F A FT-IR spectra (a) ZnONPs, (b) BC, and (c) ZnO/BC nanocomposite; B UV-visible spectra of (a) ZnONPs and (b) ZnO/BC nanocomposite; C Tauc plot of (a) ZnONPs and (b) ZnO/BC nanocomposite, D Fluorescence spectroscopy spectra for (a) ZnONPs and (b) ZnO/BC nanocomposite, E XRD pattern of ZnONPs, and F XRD patterns of (a) BC and (b) ZnO/BC nanocomposite



precursors to the acetate group [63]. The peak at 1617  $\text{cm}^{-1}$  and 1318  $\text{cm}^{-1}$  revealed symmetry and asymmetry stretching vibration of C=O bands, a smaller peak at 1016  $\text{cm}^{-1}$  was related to C-O stretching vibration, and a sharp peak at 902  $\text{cm}^{-1}$  was due to C-O bending vibration [64]. A high-intensity peak at 502  $\text{cm}^{-1}$  detected the stretching vibration of the Zn-O band as shown in Fig. 1A (a) [65]. Figure 1A (b) shows that the peaks of BC shifted peak position at 3307  $\text{cm}^{-1}$  due to O-H stretching vibration and other peaks increased intensity compared to ZnONPs. An additional peak appeared at 1722  $\text{cm}^{-1}$  due to C=O stretching vibration in the COOH group of BC as shown in Fig. 1A (b). In Fig. 1A (c), the FT-IR spectrum of the ZnO/BC nanocomposite is depicted, revealing a reduction in peak intensity along with the presence of certain peaks. Notably, shifts in peak positions are observed at 3321  $\text{cm}^{-1}$ , 1742  $\text{cm}^{-1}$ , and 427  $\text{cm}^{-1}$ , accompanied by reduced intensity. This observation indicates the successful coating of BC with ZnO, as evidenced by alterations in peak positions corresponding to O-H, C=O, and Zn-O bonding [66, 67]. The FT-IR spectra indicate that the functional groups in the BC may have contributed to the formation of the ZnO/BC nanocomposite. Table 1 presents the functional groups corresponding to the FT-IR peaks.

### 3.2 UV-visible characterization

UV-visible absorption spectra of ZnONPs and ZnO/BC nanocomposite are shown in Fig. 1B (a, b). Figure 1B (a) shows a sharp absorption peak at 372 nm, which has been described as an intrinsic transition between the valence band (O 2p orbitals) and the conduction band of ZnONPs [80, 81]. Figure 1B (b) shows that the ZnO/BC nanocomposite is shifted to a slightly longer wavelength at 382 nm with lower

bandgap energy due to more optically active centers, excitonic-related recombination, and surface traps [82]. Hence, BC is coated on ZnO to improve light harvesting, which is an essential requirement for enhancing photocatalytic activity. Figure 1C (a–c) shows the Tauc plots of ZnONP and ZnO/BC nanocomposite with calculated bandgap energy of 3.04 eV and 2.89 eV, respectively, which are correspond to previous reported results [83]. ZnO/BC nanocomposite has lower bandgap energy than ZnONPs, records a lower electron-holes recombination rate, and is more useful for visible light photocatalysts. ZnO/BC nanocomposite can improve optical properties and enhance the photocatalytic degradation of MB under sunlight irradiation [84].

### 3.3 Fluorescence spectroscopy characterizations

Defect energy levels, surface vacancies, and charge transfer of photocatalysts were identified by fluorescence spectroscopy [85]. Figure 1D (a, b) shows the fluorescence spectra of ZnONPs and ZnO/BC nanocomposite with excitation at 350 nm and is important for determining the fluorescence properties. Figure 1D (a) shows that the FL spectrum of ZnONPs observed a higher emission peak at 445 nm which is attributed to the oxygen vacancies ( $V_o$ ) in the valence band transition. The FL spectrum of ZnO/BC nanocomposite shows a low-intensity peak at 385 nm, indicating near-band-edge emission due to the mixing of electrons from the less conduction band with holes of the valence band of ZnONPs as shown in Fig. 1D (b). FL spectra of ZnONPs and ZnO/BC nanocomposite reveal lower intensity peak due to BC and quenching fluorescence properties in ZnONPs. Low fluorescence indicates charge transfer and a reduced rate of electron-hole recombination

**Table 1** Functional groups of ZnONPs, BC, and ZnO/BC nanocomposite were determined by FT-IR

| FT-IR wave number ( $\text{cm}^{-1}$ ) | Vibrations   | References |
|--|--|------------|
| <b>ZnONPs</b>                          |  |            |
| 3404 $\text{cm}^{-1}$                  | O-H stretching vibration                           | [68]       |
| 2931 and 2855 $\text{cm}^{-1}$         | C-H stretching—methyl and methylene groups         | [69]       |
| 1617 $\text{cm}^{-1}$                  | C=O stretching—carboxylic group                    | [70]       |
| 1318 $\text{cm}^{-1}$                  | symmetry stretching vibration C=O                  | [71]       |
| 1016 $\text{cm}^{-1}$                  | C-O stretching—saturated ester                     | [72]       |
| 902 $\text{cm}^{-1}$                   | C-O bending vibration                              | [73]       |
| 502 $\text{cm}^{-1}$                   | Zn-O stretching vibration                          | [74]       |
| <b>Biochar (BC)</b>                    |  |            |
| 3307 $\text{cm}^{-1}$                  | O-H stretching—carboxylic acid and hydroxyl groups | [75]       |
| 1722 $\text{cm}^{-1}$                  | O-C=O stretching vibration in the COOH group       | [76]       |
| <b>ZnO/BC nanocomposite</b>            |  |            |
| 3321 $\text{cm}^{-1}$                  | O-H stretching in hydroxyl groups and phenol       | [77]       |
| 1742 $\text{cm}^{-1}$                  | -C=O stretching—carboxylic group                   | [78]       |
| 427 $\text{cm}^{-1}$                   | Zn-O stretching vibration                          | [79]       |

[86, 87]. As a result, the ZnO/BC nanocomposite has excellent photocatalytic activity under sunlight irradiation.

### 3.4 XRD characterizations

Powder X-ray diffraction serves as an effective method for examining both amorphous and crystalline aspects of prepared materials. As depicted in Figure 1E (a), the XRD pattern of the pure ZnO nanoparticles (ZnONPs) displays a set of distinct diffraction peaks. Notably, these peaks are identified at specific angles: 31.78° (100), 34.26° (002), 36.25° (101), 47.56° (102), 56.75° (110), 62.75° (103), 66.37° (200), 67.95° (112), 69.33° (201), 72.48° (004), and 76.93° (202). These discernible peaks unequivocally indicate the presence of the wurtzite structure characteristic of ZnO. The alignment of these peaks corresponds precisely to the JCPDS card no. 36-1451. Importantly, the observed peaks provide strong evidence of the material's well-defined crystalline nature [88]. Figure 1F (a, b) shows the X-ray diffraction pattern of BP powder and ZnO/BC nanocomposite. Several peaks were assigned to BP powder, of which two major peaks corresponded to the (002) and (100) plane of disordered graphitic carbon at  $2\theta$  of 21.34° and 40.29° in BC as identified by the JCPDS card no. 46-1045 as shown in Fig. 1F (a) [89–91]. Figure 1E (b) shows the XRD pattern of the ZnO/BC nanocomposite, which shows peaks indicating the crystallinity of the variants at 28.13°, 31.86°, 34.39°, 47.58°, 62.48°, and 66.35° with corresponding to (111), (100), (002), (102), (103), and (200) crystalline planes [92, 93]. Additionally, these peaks were observed as ZnONPs according to the JCPDS card no. 36-1451. Two prominent peaks appear at  $2\theta = 21.34^\circ$ , accompanied by a less pronounced peak at  $2\theta = 40.29^\circ$ , corresponding to the C (002) and C(100) planes, respectively. This unmistakably signifies the presence of a graphitic structure within the biochar (BC). Furthermore, a sharp peak of significant intensity appears at 28.13° along the (111) plane, indicating that the crystallinity patterns of the BC structure became more defined after forming the ZnO/BC nanocomposite [94, 95]. This result suggests that the ZnO/BC nanocomposite was effectively synthesized using ZnONPs and BC biochar. The average size of the ZnONPs within the ZnO/BC nanocomposite was determined from the maximum crystalline peak of ZnO at 31.86°, which corresponds to the (101) plane. To compute this size, the Debye-Scherrer formula was employed, as outlined by the equation:

$$D = 0.9 \lambda / \beta \cos\theta \quad (3)$$

where 0.9 is the shape factor,  $\lambda$  is the x-ray wavelength ( $\lambda=1.5418 \text{ \AA}$ ),  $\beta$  is the line broadening at half-width maximum intensity (FWHM) in radians, and  $\theta$  is the Bragg angle. The average size of the ZnO nanoparticles was found to be

18 nm. For the ZnO/BC nanocomposite, the average size was calculated at the  $2\theta$  position of the (101) peak of ZnO NPs, which was 30 nm.

### 3.5 SEM characterizations

Scanning electron microscope was used to find the surface morphology structure and shape of materials. Figure 2A–C shows the SEM images of small ZnONP aggregate with a granular shape at increasing magnifications of (A) 12 kV, 1.15 kx, (B) 12.0 kV, 3.09 kx, and (C) 12.0 kV, 5.12 kx. The EDAX spectrum for elemental determination of Zn and O in ZnONPs was revealed as shown in Fig. 2D. Figure 3A–C shows the SEM image of ZnO/BC nanocomposite at different magnifications of (A) 20.0 kV, 1.50 kx, (B) 20.0 kV, 6.76 kx, and (C) 20.0 kV, 17.7 kx. The nanocomposite at 1.50 kx magnification looks like white particles of ZnO coated on the integrated structure of biochar and irregular size particles are recorded as shown in Fig. 3A. At 6.76 kx magnification it looks like irregular stalks of white particles clustered together irregularly as shown in Fig. 3B. At a higher magnification of 17.7 kx, it clearly shows the irregularly shaped rod and particles as shown in Fig. 3C. EDAX spectrum confirmed the Zn, O, and C elements ZnO/BC nanocomposite as shown in Fig. 3D.

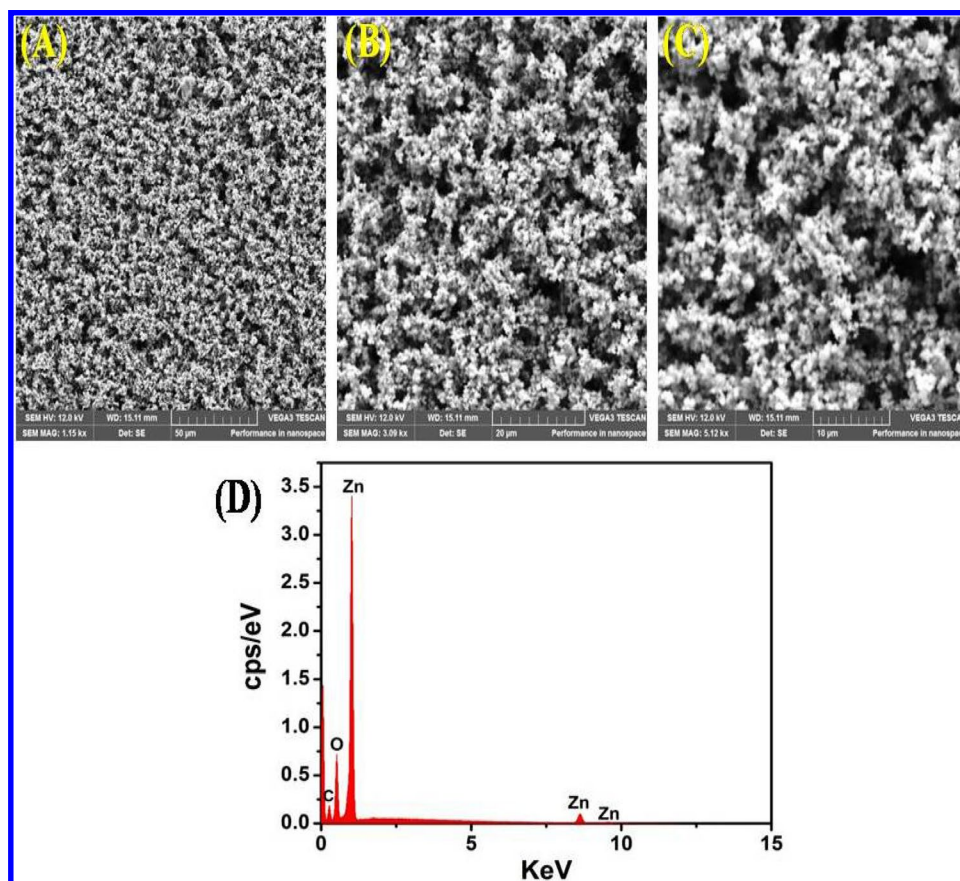
### 3.6 TEM characterizations

Figure 4A–D shows the TEM images of ZnO (A, B) and ZnO/BC nanocomposite (C, D) at magnifications of (A) 65 kx (200 nm scale bar), (B) 100 kx (100 nm scale bar), and 60 kx (50 nm scale bars insets to both A and B). Distinct shapes of ZnO nanoparticles (ZnONPs) were clearly evident under different magnifications, 65 kx and 100 kx, as illustrated in Fig. 4A and B. At the higher magnification of 60 kx, the hexagonal and square configurations of ZnONPs were captured and are featured in Fig. 4A and B, respectively. These images decisively affirmed the successful synthesis of ZnONPs through the hydrothermal method.

Figure 4C and D presents the images of the ZnO/biochar (ZnO/BC) nanocomposite. In Fig. 4C, observed at 100 kx with a 200-nm scale bar, agglomerated structures integrated with dark particles coated on the biochar substrate are discernible. This amalgamation is attributed to the ZnONPs and BC components. Similarly, Fig. 4D portrays the nanocomposite at 140 kx with a 100 nm scale bar, further highlighting the distinctive features of ZnONPs and BC.

Collectively, these visual representations provide conclusive evidence of the successful formation of ZnONPs and the ZnO/BC nanocomposite using the hydrothermal method. The size of the ZnO/BC nanocomposite, ranging approximately between 20 and 30 nm, was found to be in close agreement with the XRD analysis. This alignment further

**Fig. 2** A–D SEM images of synthesized ZnONPs with different magnifications A 50  $\mu\text{m}$ , B 20  $\mu\text{m}$ , and C 10  $\mu\text{m}$  and D EDAX spectrum of ZnONPs



validates the successful encapsulation of the BP biochar within the ZnO nanoparticles (ZnONPs).

### 3.7 Photocatalytic degradation studies

The evaluation of catalyst-free photocatalytic degradation involved three scenarios: only sunlight, sunlight with ZnO nanoparticles (Sunlight + ZnONPs), and sunlight with the ZnO/biochar nanocomposite (Sunlight + ZnO/BC), targeting the degradation of methylene blue (MB) using UV-visible spectroscopy. In the standard procedure, the photocatalysts were subjected to a preliminary MB photocatalytic degradation study in the absence of light for 30 minutes to confirm the adsorption/desorption process, which served as the 0-minute reference. Subsequently, UV-visible spectral analysis was used to monitor the progress of MB photocatalytic degradation under sunlight irradiation.

Without a catalyst, the UV-visible spectra of MB showed a persistent peak at 662 nm, indicating incomplete reduction in intensity across the time intervals from 0 to 120 min, as illustrated in Fig. 5A. Introducing ZnONPs as the catalyst exhibited a gradual reduction in the UV-visible spectrum of MB under sunlight irradiation over the same time range, as depicted in Fig. 5B. In contrast, the ZnO/BC nanocomposites proved particularly efficient in degrading

MB under sunlight irradiation within the 0 to 120-min span, evident in both the spectral data displayed in Fig. 5C and the inset digital images.

The assessment of photocatalytic efficiency was quantified as depicted in Fig. 5D (a–c), which illustrates the percentage degradation of MB under sunlight irradiation, comparing the scenarios of no catalyst, ZnONPs catalyst, and ZnO/BC nanocomposite catalyst at different time intervals using Equation (2). Significantly, the ZnO/BC nanocomposite demonstrated superior photocatalytic activity, exhibiting a degradation efficiency of 91%, outperforming ZnONPs (72%) and the absence of a catalyst (43%). Notably, ZnO/BC nanocomposite proved to be an exceptional photocatalyst for the degradation of MB under visible light irradiation.

Further insight into the kinetic rate constant and comparative analysis with previous literature related to ZnO nanocomposites are summarized in Tables 2 and 3. Significantly, the ZnO/BC nanocomposite displayed a higher rate constant compared to ZnONPs and the no-catalyst scenario. These findings, supported by digital images in Fig. 5F, reinforce the exceptional photocatalytic performance of the ZnO/BC nanocomposite. Notably, the behavior of the ZnO/BC nanocomposite aligns well with results reported in the existing literature, showcasing its promising potential.



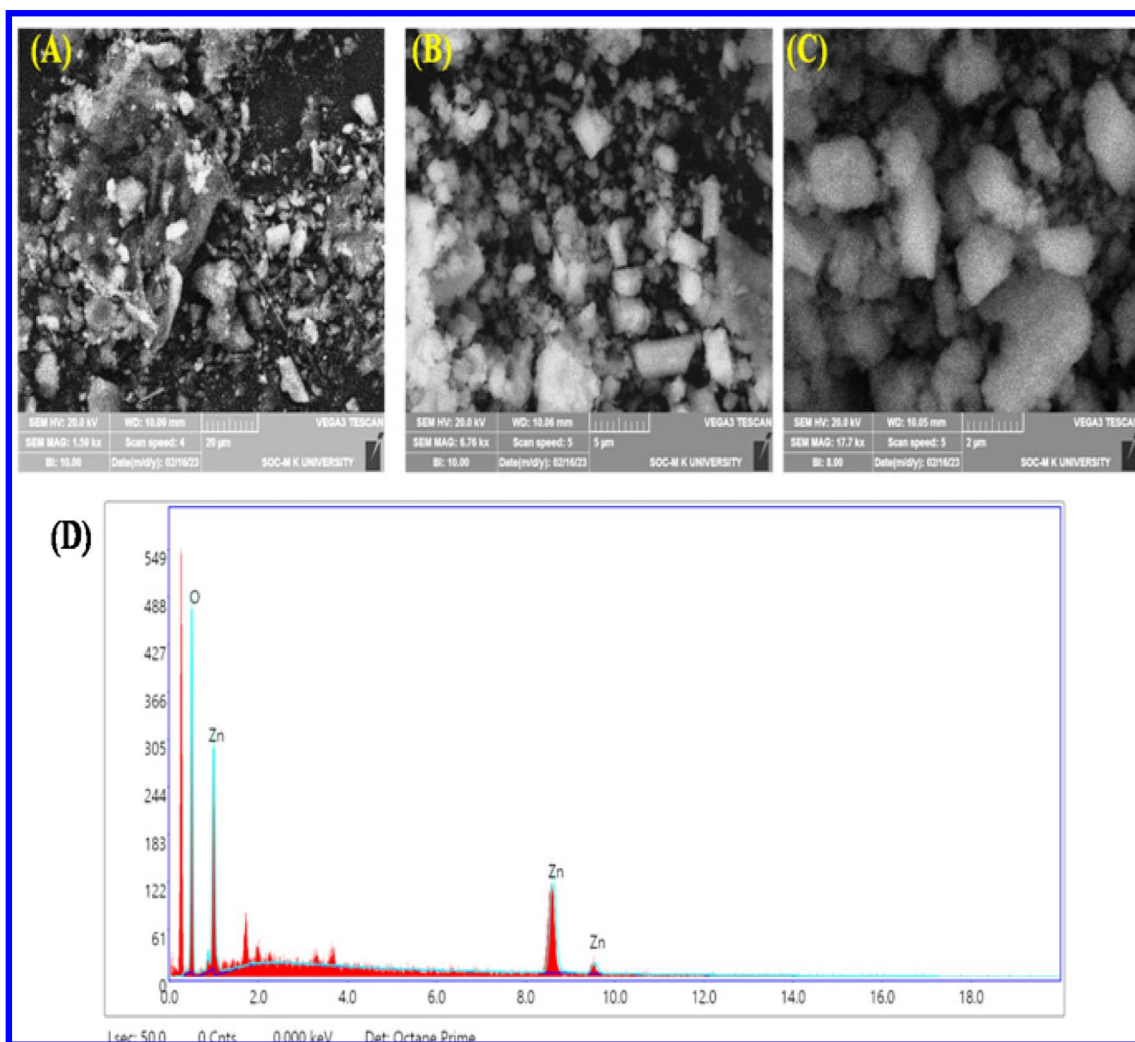


**Fig. 3** A–D SEM images of synthesized ZnO/BC nanocomposite with different magnifications **A** 20 μm, **B** 5 μm, and **C** 2 μm and **D** EDAX spectrum of ZnO/BC nanocomposite

### 3.8 Effect of photocatalyst dosages

Figure 6 presents a crucial insight into the effect of varying photocatalyst dosages on the removal of dye, particularly highlighting the significance of the 100 mg dose for achieving optimal dye removal. Figure 6A–E effectively portrays the impact of different dosage levels, ranging from 25 to 125 mg of ZnO/biochar (ZnO/BC) nanocomposite, while maintaining an initial concentration of 10 ppm of methylene blue (MB) under sunlight irradiation over a duration of 0 to 120 min.

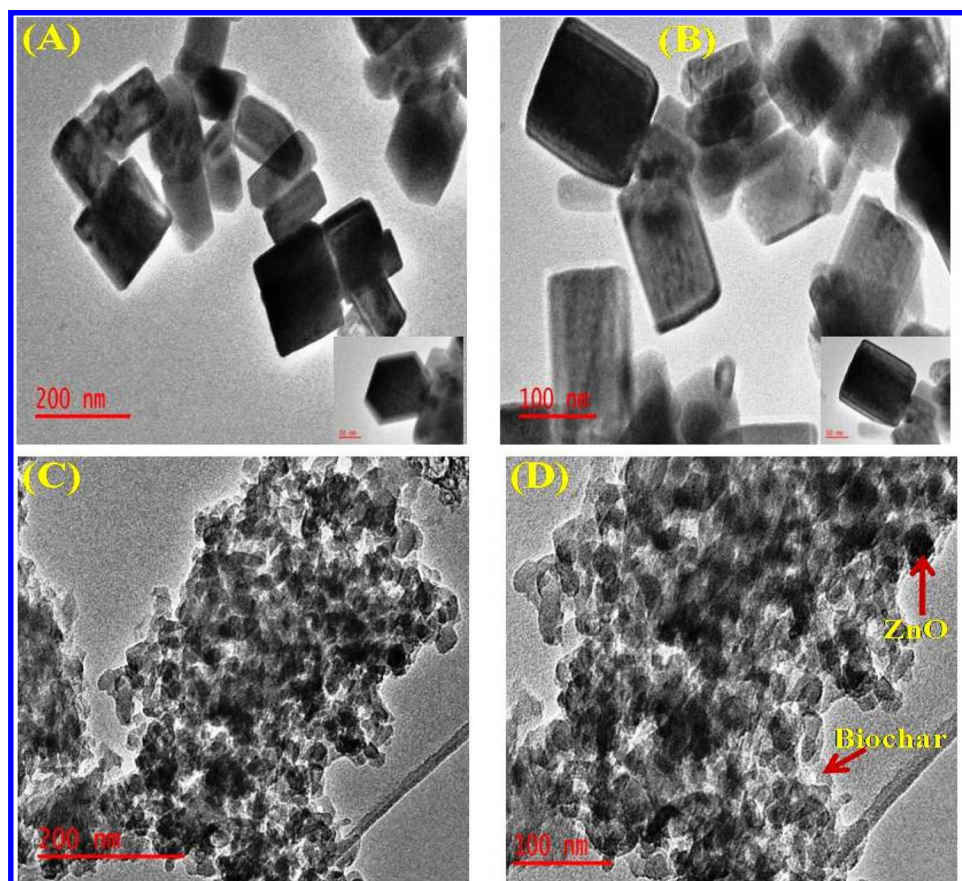
Figure 6A–C details the photocatalytic degradation of MB using ZnO/BC nanocomposite dosages of 25 mg, 50 mg, and 75 mg. Under these conditions, the degradation is incomplete due to insufficient catalyst dosages and low photocatalytic activity. In contrast, Fig. 6D and E shows the degradation patterns with 100 mg and 125 mg dosages of

ZnO/BC nanocomposite, respectively, where the photocatalytic degradations result in a nearly complete reduction in intensity over 0 to 120 min.

The efficacy of ZnO/BC nanocomposite as a photocatalyst was quantified through degradation efficiency calculations using Equation (1) for various dosages. The resulting degradation percentages for MB were 27% (25 mg), 45% (50 mg), 54% (75 mg), 91% (100 mg), and 96% (125 mg) as depicted in Fig. 6F (a–e) and summarized in Table 2. These findings corroborate that 100 mg and 125 mg dosages of ZnO/BC nanocomposite yields remarkable MB degradation under sunlight irradiation within the 0 to 120-min timeframe, attributed to the elevated concentration of active photocatalytic sites.

Furthermore, the kinetic degradation rate of MB, utilizing varying catalyst dosages of ZnO/BC nanocomposite under sunlight irradiation, was also assessed. Figure 6G

**Fig. 4** A–D TEM images of synthesized ZnONPs with different magnifications **A** 200 nm, **B** 100 nm, and 50 nm inset (**A**, **B**) and **C** 200 nm and **D** 100 nm of ZnO/BC nanocomposite



(a–e) shows the  $\ln(C_t/C_0)$  versus time plot, which was used to determine the kinetic rate constant for the photocatalytic degradation of MB using Equation (2), as detailed and summarized in Table 2.

Although the 125 mg dose shown in Fig. 6E achieved slightly higher MB removal, it was slower in the initial phase of degradation. Therefore, the 100 mg dosage provided a better balance between removal rate and degradation efficiency, resulting in the rapid decolorization of the MB dye within 0 to 100 min under visible light irradiation.

### 3.9 Effect of MB concentration

The impact of varying concentrations of methylene blue (MB)—5 ppm, 15 ppm, 20 ppm, and 25 ppm—on the photocatalytic efficacy when coupled with ZnO/biochar (ZnO/BC) nanocomposite (100 mg) under sunlight irradiation at different time intervals (0 to 120 min) is visualized in Fig. 7A–D.

Figure 7A distinctly depicts the ongoing, continuous decrease in photocatalytic degradation intensity of MB (5 ppm) when treated with ZnO/BC nanocomposite under sunlight irradiation from 0 to 60 min. This contrastingly progressive trend differentiates it from the concentrations of 15 ppm, 20 ppm, and 25 ppm, as illustrated in Fig. 7B–D. The higher concentrations of 20 ppm and 25 ppm, however,

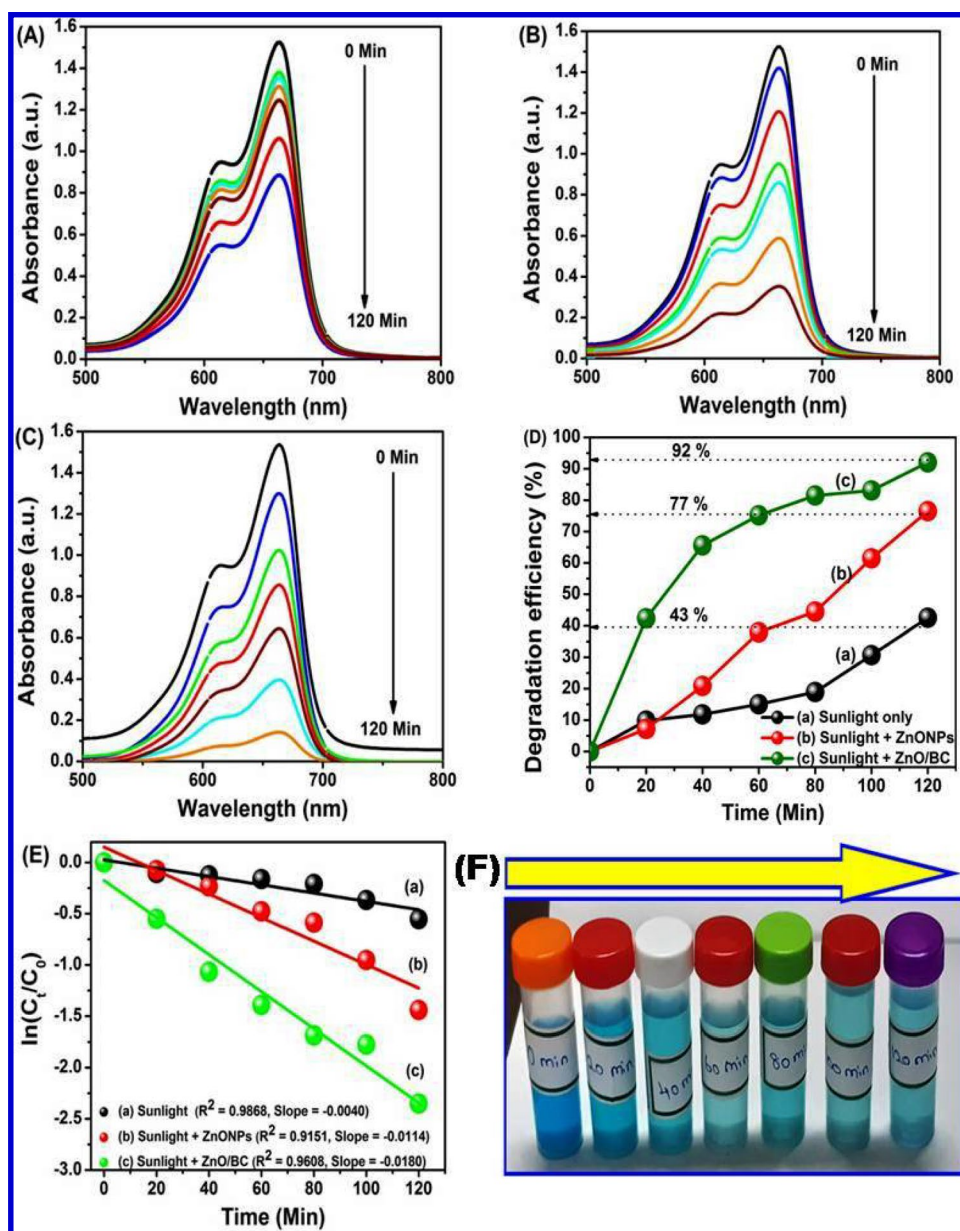
exhibited slower degradation rates under sunlight irradiation over the 0 to 120-min duration. This deceleration can be attributed to the abundant presence of MB molecules, which absorb significant sunlight and impede irradiation. As represented in Fig. 7C and D, this light absorption behavior aligns with the observed trend [100].

Quantitatively, the percentages of MB degradation were found to be 98%, 87%, 68%, and 45% for concentrations of 5 ppm, 15 ppm, 20 ppm, and 25 ppm, respectively, as demonstrated in Fig. 7E. Furthermore, the kinetic rate constants, obtained from the analysis illustrated in Fig. 7F, are summarized in Table 2. The results underscore the exceptional degradation efficiency and kinetic rate constant achieved at a concentration of 5 ppm, highlighting its optimal performance.

#### 3.9.1 Effect of pH

The treatment of wastewater involves a broad spectrum of pH values that influence pollutant removal through photocatalytic degradation, mediated by the catalysts' surface charge. Investigation into these pH conditions (pH 3, 5, 8, and 10) involved the ZnO/biochar (ZnO/BC) nanocomposite (100 mg) as a photocatalyst, targeting the degradation of methylene blue (MB) at a concentration of 10 ppm. These

**Fig. 5** A–F UV-visible absorption spectra of MB with **A** catalyst free; **B** ZnONPs and **C** ZnO/BC nanocomposite with photocatalytic degradation of MB under sunlight irradiation at 0 to 120 min; **D** plot of the percentage of degradation efficiency vs. time (a) catalyst free, (b) ZnONPs, and (c) ZnO/BC nanocomposite; **E** plot of  $\ln(C_t/C_0)$  vs. time (a) catalyst free, (b) ZnONPs, and (c) ZnO/BC nanocomposite; and **F** digital image of successive photocatalytic degradation of MB with ZnO/BC nanocomposite



studies were conducted under sunlight irradiation, spanning time intervals of 0 to 120 minutes, as elucidated in Fig. S1 (A–D) within the supporting information.

Figure S1 (A, B) captures the photocatalytic degradation spectra of MB at pH 3 and pH 5, revealing that the peak intensity reduction is incomplete. This phenomenon arises from the repulsion between the positive charge of the ZnO/BC nanocomposite and the positive charge of MB [101]. At lower pH values, specifically 3 and 5, the ZnO/BC nanocomposite exhibits a positive surface charge due to the high concentration of  $H^+$  ions. This results in reduced MB dye adsorption and lower photocatalytic degradation efficiency, as the electrostatic repulsion between MB and the ZnO/BC nanocomposite

diminishes the interaction [102]. In contrast, the photocatalytic process gains momentum at pH 8, as depicted in Fig. S1 (C), where MB undergoes degradation under sunlight irradiation within the 0 to 120-min interval. This shift is attributed to the attractive interplay between the negative charges of the ZnO/BC nanocomposite at higher amount of  $OH^-$  ions, which can interact with the positive charge of MB for electrostatic attraction [103]. Similarly, Fig. S1 (D) underscores the consistent degradation of MB at pH 10 and the result of electrostatic attraction between the highly negative charge of the ZnO/BC nanocomposite and the positive charge of MB. Moreover, the ZnO/BC nanocomposite surface is predominantly occupied by hydroxyl and oxygen groups at higher pH 8 and pH 10,

**Table 2** Summary of degradation efficiency and rate constants for photocatalytic degradation of MB under varying experimental conditions

| Nanocomposites    | Dosages (mg) | MB concentration (ppm) | pH | Scavenger   | Degradation efficiency (%) | Rate constant (k) (min <sup>-1</sup> ) | R <sup>2</sup> |
|-------------------|--------------|------------------------|----|---|----------------------------|--|----------------|
| Sunlight only     | -            | 10                     | -  | -   | 43%                        | 0.0040                                 | 0.9868         |
| Sunlight + ZnONPs | 100          |                        |    |   | 77%                        | 0.0114                                 | 0.9151         |
| Sunlight + ZnO/BC | 125          |                        |    |   | 96 %                       | 0.0340                                 | 0.9218         |
|                   | 100          |                        |    |   | 92%                        | 0.0180                                 | 0.9608         |
|                   | 75           |                        |    |   | 54%                        | 0.0087                                 | 0.9282         |
|                   | 50           |                        |    |   | 45%                        | 0.0056                                 | 0.9609         |
|                   | 25           |                        |    |   | 27%                        | 0.0042                                 | 0.9921         |
|                   | 100          | 25                     |    |   | 45%                        | 0.009                                  | 0.8854         |
|                   |              | 20                     |    |   | 68%                        | 0.0178                                 | 0.8751         |
|                   |              | 15                     |    |   | 87%                        | 0.0248                                 | 0.9472         |
|                   |              | 5                      |    |   | 98%                        | 0.0603                                 | 0.8816         |
|                   |              | 10                     |    | 3   |                            | 40%                                    | 0.0527         |
|                   |              |                        | 5  |   | 65%                        | 0.00705                                | 0.9542         |
|                   |              |                        | 8  |   | 85%                        | 0.01429                                | 0.7702         |
|                   |              |                        | 10 |   | 94%                        | 0.0233                                 | 0.9119         |
|                   |              |                        | -  | EDTA (h <sup>+</sup> )  | 90%                        | 0.0193                                 | 0.9516         |
|                   |              |                        |    | Na <sub>2</sub> SO <sub>4</sub> (e <sup>-</sup> )                           | 66 %                       | 0.0095                                 | 0.8432         |
|                   |              |                        |    | IPA ( <sup>•</sup> OH)  | 55 %                       | 0.0068                                 | 0.8651         |
|                   |              |                        |    | H <sub>3</sub> PO <sub>4</sub> ( <sup>•</sup> O <sub>2</sub> <sup>-</sup> ) | 36%                        | 0.0037                                 | 0.9899         |

**Table 3** Comparison of photocatalytic degradation of MB with ZnO-biochar-based nanocomposites

| Nanocomposites                              | Light source                   | Degradation efficiency (%) | References |
|---|--------------------------------|----------------------------|------------|
| ZnO-/carbon-based material                  | Ultraviolet (UV)               | 95                         | [96]       |
| ZnO/biochar nanocomposites                  | Visible light                  | 95.19                      | [67]       |
| ZnO/biochar                                 | Ultraviolet (UV)               | 99                         | [97]       |
| ZnO-C nanocomposite                         | Visible light                  | 99.7                       | [98]       |
| ZnO/biochar nanocomposites                  | Ultraviolet (UV)               | 83.1                       | [43]       |
| Zinc oxide-N, O-contained biochar (ZnO/NOC) | ultraviolet and visible lights | 93                         | [99]       |
| Biochar impregnated with ZnO nano-flowers   | Natural sunlight               | 94                         | [55]       |

and surface charges exist as negative values [104]. This nanocomposite showed more affinity toward cationic MB dye, which is necessary for better adsorption in order to achieve increased photocatalytic degradation [105].

The pivotal role of pH 10 is evident, where the photocatalytic degradation of MB with the ZnO/BC nanocomposite takes precedence under sunlight irradiation. Substantiating this, the percentage (%) degradation efficiency of MB is quantified in Fig. 8A (a–d), yielding values of 40%, 65%, 85%, and 94% at pH levels of 3, 5, 8, and 10, respectively. Decay kinetic rate constants were calculated using  $\ln(C_t/C_0)$  versus times and various pHs 3,5,8 and 10 as shown in Fig. 8B (a–d) and reported in Table 2. Interestingly, the best degradation efficiency and kinetic rate constant were demonstrated at pH 10.

### 3.9.2 Effect of scavengers' studies

Within the framework of this photocatalytic investigation, diverse scavengers were employed to quench reactive species, constituting a vital facet of the experimental procedure. The assessment of photocatalytic activity entailed a range of scavenger probes, each strategically incorporated. In the context of the photocatalytic degradation of methylene blue (MB) at a concentration of 10 ppm, specific scavengers were harnessed to target distinct species. Isopropanol (IPA), hydrogen phosphate (H<sub>3</sub>PO<sub>4</sub>), ethylenediaminetetraacetic acid (EDTA), and sodium persulfate (Na<sub>2</sub>S<sub>2</sub>O<sub>8</sub>) were adeptly chosen as effective quenchers for hydroxide radicals (<sup>•</sup>OH), superoxide radicals (<sup>•</sup>O<sub>2</sub><sup>-</sup>), holes (h<sup>+</sup>), and electrons (e<sup>-</sup>) [106–108]. These reactive species

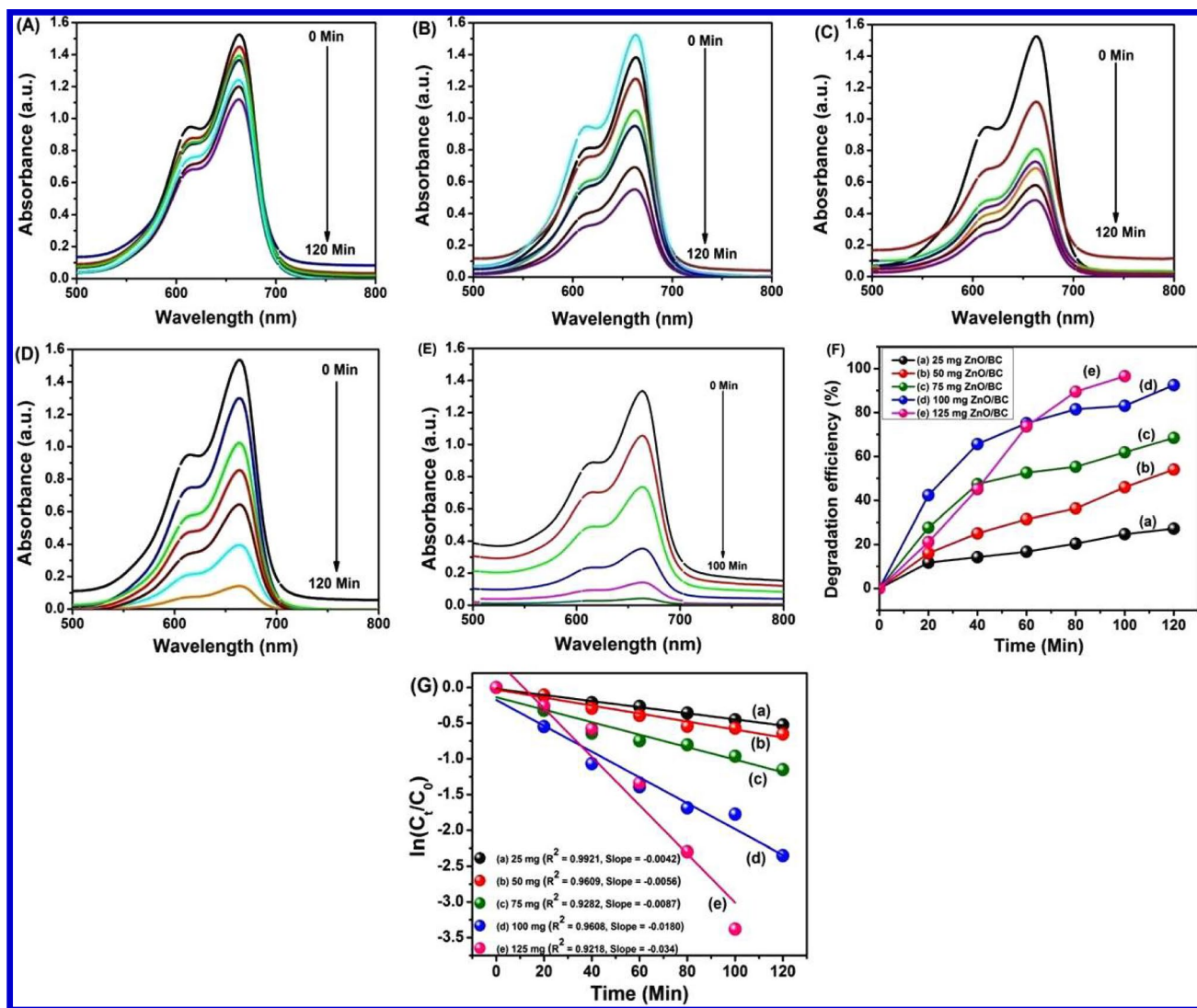


**Fig. 6** A–G UV-visible absorption spectra of MB with different dosages of **A** 25 mg, **B** 50 mg, **C** 75 mg, **D** 100 mg, and **E** 125 mg with ZnO/BC nanocomposite under sunlight irradiation. **F** Plot of degrada-

tion efficiency (%) and **G** plot of  $\ln(C_t/C_0)$  vs time of (a) 25 mg, (b) 50 mg, (c) 75 mg, (d) 100 mg, and (e) 125 mg

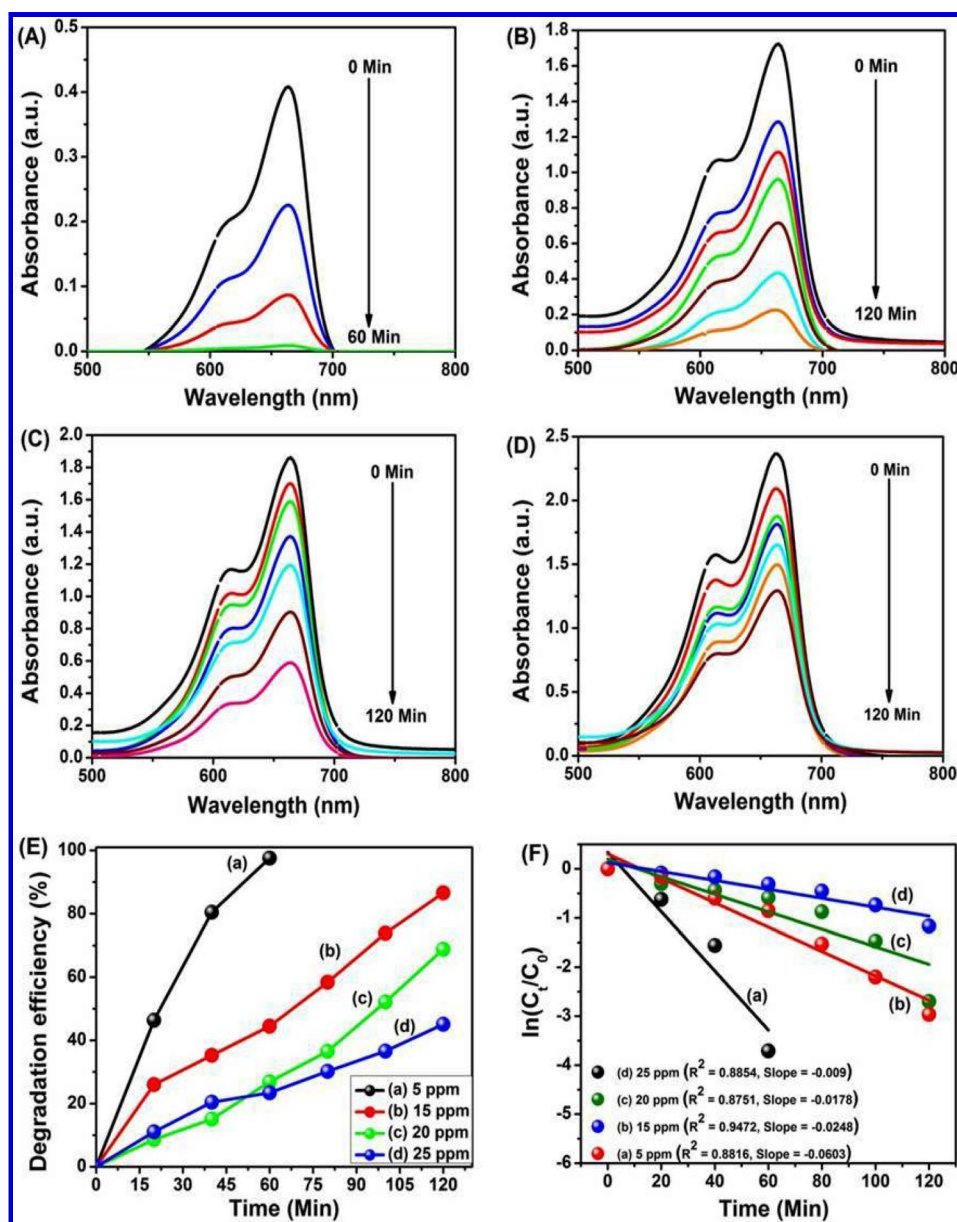
manifest during the photocatalytic degradation of MB under sunlight irradiation.

Interestingly, both EDTA and  $\text{Na}_2\text{S}_2\text{O}_8$  exhibited limited interaction with the holes ( $h^+$ ) and electrons ( $e^-$ ) emanating from the ZnO/BC nanocomposite during the photocatalytic degradation of MB under sunlight irradiation over the 0 to 120-min span. Conversely, holes ( $h^+$ ) and electrons ( $e^-$ ) emerged as the primary agents driving the degradation of MB, accounting for respective percentage degradation efficiencies of 90 % and 66 %, as presented in Fig. 8C (a, b). Intriguingly, the scavengers IPA (55%) and  $\text{H}_3\text{PO}_4$  (36%) displayed comparatively lesser involvement in the photocatalytic degradation of MB in conjunction with the ZnO/BC nanocomposite under sunlight

irradiation as shown in Fig. 8C (c, d). Notably, hydroxide radicals ( $\bullet\text{OH}$ ) and superoxide radicals ( $\bullet\text{O}_2^-$ ) were more significantly scavenged, as delineated in Fig. 8C (c, d).

The determination of the kinetic rate constant ( $k$ ) was derived from the plot of  $\ln(C_t/C_0)$  versus time ( $t$ ), and slope analysis facilitated the extraction of pertinent information, as illustrated in Fig. 8D (a–d). The derived values, including  $R^2$  and  $k$  reported in Table 2, unveiled the kinetic characteristics of the scavengers. Specifically, the high degradation rate constants of EDTA and  $\text{Na}_2\text{S}_2\text{O}_8$  were particularly noteworthy, further attesting to their efficacy in degrading MB. The intricate interplay between scavengers and photocatalytic reactions thus adds a layer of understanding to the complex degradation process.

**Fig. 7** A–F UV-visible absorption spectra of MB with different concentration of **A** 5 ppm, **B** 15 ppm, **C** 20 ppm, and **D** 25 ppm with ZnO/BC nanocomposite under sunlight irradiation. **E** Plot of degradation efficiency (%) and **F** plot of  $\ln(C_t/C_0)$  vs time of (a) 5 ppm, (b) 15 ppm, (c) 20 ppm, and (d) 25 ppm



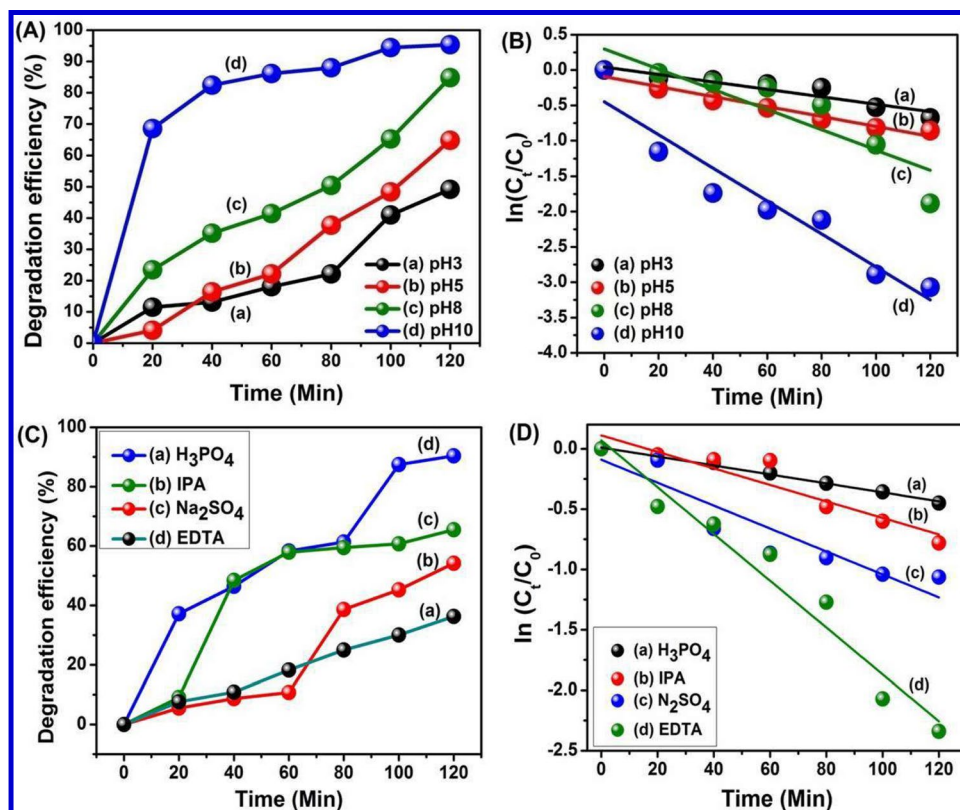
### 3.9.3 Stability and reusability of studies

The assessment of stability and reusability of the photocatalysts centered on the photocatalytic degradation of methylene blue (MB) at a concentration of 10 ppm, employing the ZnO/biochar (ZnO/BC) nanocomposite (100 mg) under sunlight irradiation spanning 0 to 120 min. Upon completion of the photocatalytic degradation experiment, the ZnO/BC nanocomposite photocatalyst was extracted and separated via centrifugation. It underwent rigorous washing with water and ethanol, followed by drying in a high-temperature oven set at 60°C. Subsequently, the photocatalyst was introduced into a freshly prepared MB solution of the same concentration. This procedure was iteratively executed across 4

consecutive cycles, each encompassing the photocatalytic degradation of MB under sunlight irradiation for durations spanning 0 to 120 min, as depicted in Fig. 9A–D.

From the plot portraying (%) removal efficiency against the number of cycles, distinct percentages of degradation efficiency were garnered: 92%, 90%, 75%, and 55%. Remarkably, the photocatalytic degradation efficiencies remained relatively steady at 55% even after the completion of four cycles, underscoring the sustained performance of the ZnO/BC nanocomposite, as showcased in Fig. 9E. A small quantity of catalyst lost during the regeneration process can be used to explain this slight decrease in photocatalytic degradation efficiency [109]. This observation definitively attests to the commendable stability and reusability of the ZnO/BC

**Fig. 8** A–D **A** Degradation efficiencies and **B** plot of kinetic rate constants of MB (a) pH 3, (b) pH 5, (c) pH 8, and (d) pH 10. **C** Degradation efficiencies and **D** plot of kinetic rate constants of various scavengers (a)  $\text{H}_3\text{PO}_4$ , (b) IPA, (c)  $\text{Na}_2\text{SO}_4$ , and (d) EDTA under sunlight irradiation with ZnO/BC nanocomposite



nanocomposite in the context of photocatalytic MB degradation. Figure 9F (a, b) shows the Fourier-transform infrared (FT-IR) spectra of the ZnO/BC nanocomposite, both before and after the photocatalytic degradation of MB. The results indicate that the spectra exhibit limited alteration following the photocatalytic degradation experiment. This corroborates the persistence of the ZnO/BC nanocomposite compositional integrity and structural attributes throughout the course of the photocatalytic process.

### 3.9.4 Photocatalytic degradation mechanism of MB with ZnO/BC nanocomposite

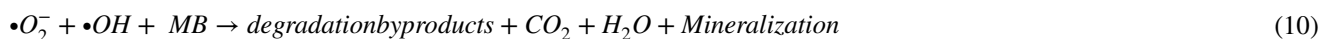
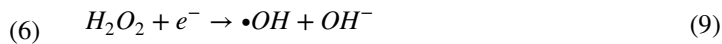
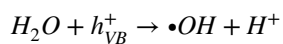
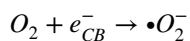
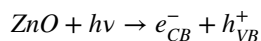
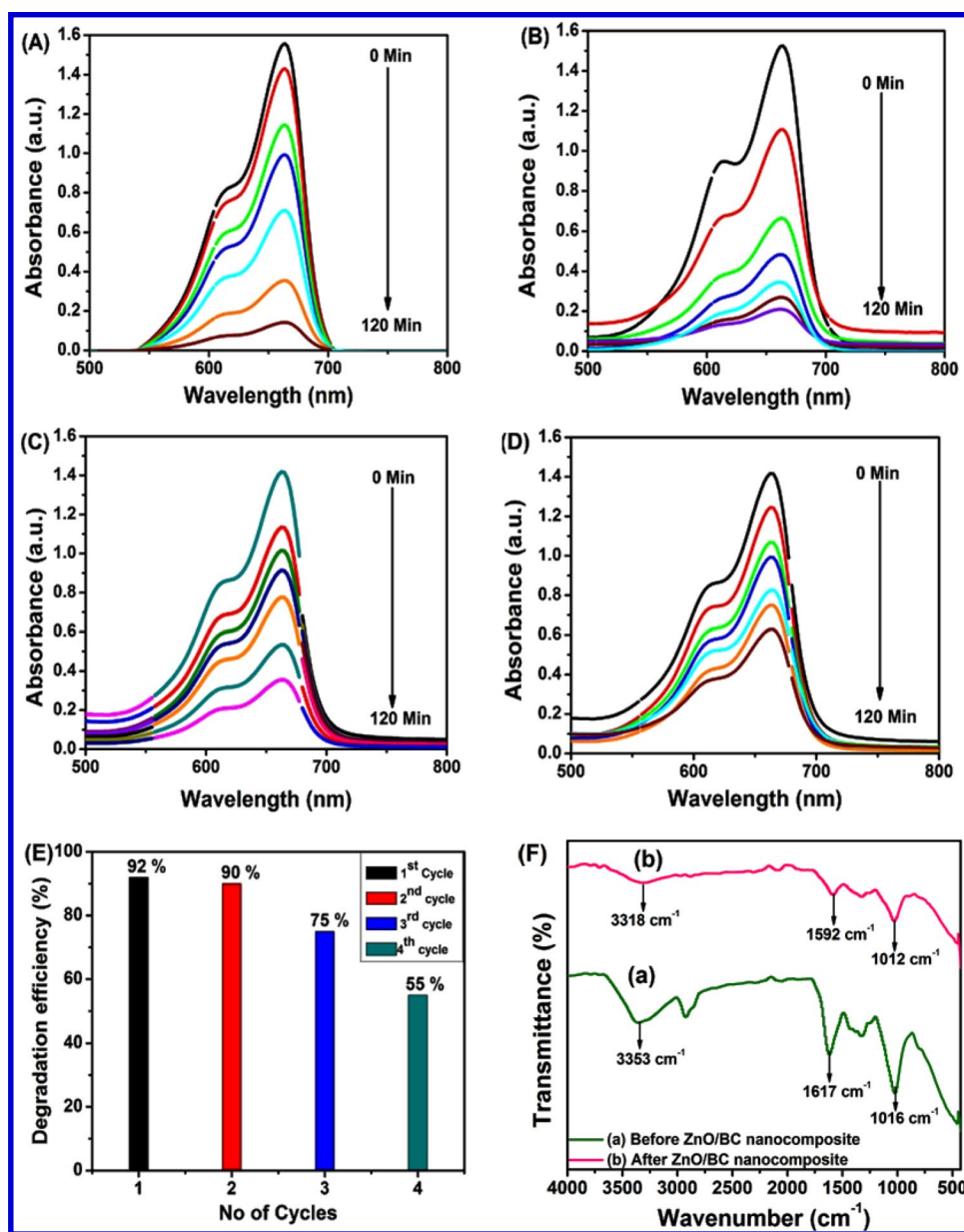
Under sunlight, the ZnONPs photocatalyst prompts the excitation of electrons from the valence band (VB) of ZnO to their conduction band (CB), accompanied by the generation of photogenerated holes. These photogenerated electrons are subsequently captured by dissolved oxygen molecules in water, leading to the formation of superoxide radical anions ( $\bullet\text{O}_2^-$ ). Simultaneously, the photogenerated holes interact with hydroxyl ions, resulting in their absorption onto the photocatalyst's surface, yielding hydroxyl radicals ( $\bullet\text{OH}$ ). These hydroxide radicals ( $\bullet\text{OH}$ ) and superoxide radical anions ( $\bullet\text{O}_2^-$ ) are thought to play a role in the degradation of MB and its eventual mineralization [110, 111].

Nevertheless, the facile recombination of these photocatalytically generated electron and hole pairs, due to the significant energy gap (3.04 eV), hampers the overall photocatalytic

efficiency of the pristine ZnO catalyst. In contrast, the ZnO/BC nanocomposite (with a narrower energy gap of 2.89 eV) capitalizes on the synergistic effect of ZnO and biochar during the MB degradation process. Upon UV-visible light irradiation, ZnO nanoparticles become activated, inducing the generation of photogenerated electron-hole pairs. Furthermore, the establishment of Zn-O-C bonds, as depicted in the diagram, facilitates the transfer of electrons from the ZnO nanoparticles conduction band to the biochar surface [112]. This notably reduces the recombination rate of the generated  $e^-/h^+$  pairs within the ZnO/BC nanocomposite. The ZnO/BC nanocomposite FT-IR spectrum following MB degradation showed three prominent peaks with clearly visible decreased intensity and shifted wave number as demonstrated in Fig. 9F (b). The attachment of MB to the BC in the ZnO/BC nanocomposite was responsible for the peak intensity and shifts at  $3318\text{ cm}^{-1}$ ,  $1592\text{ cm}^{-1}$ , and  $1012\text{ cm}^{-1}$ , which corresponded to the O-H bond, C=O bond, and C-O bond of BC in the nanocomposite [113, 114].

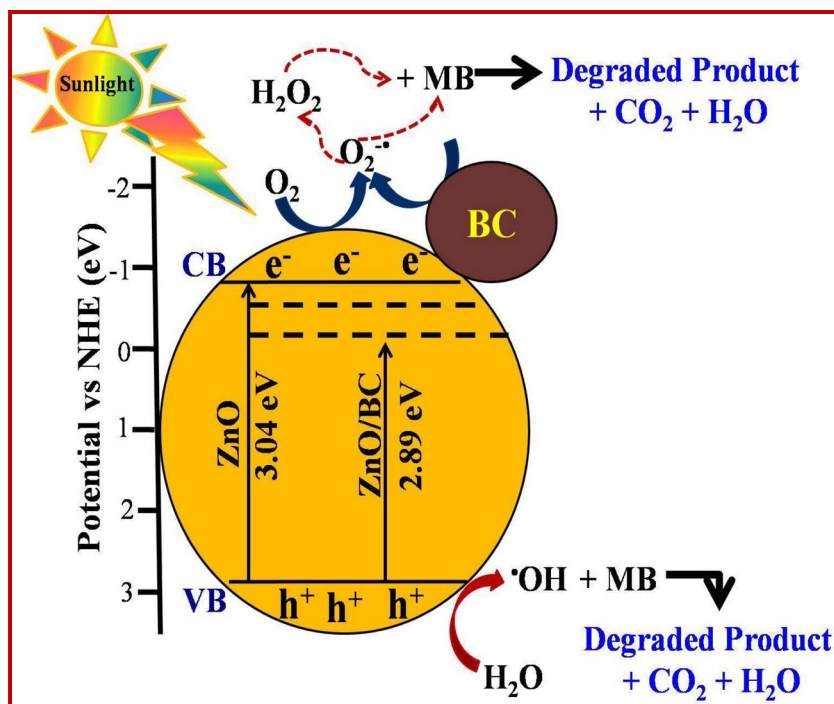
Moreover, the conduction band electrons ( $e^-$ ) of biochar react with oxygen ( $\text{O}_2$ ) to form superoxide radicals ( $\bullet\text{O}_2^-$ ), while the valence band holes ( $h^+$ ) of ZnO contribute to the generation of hydroxide radicals ( $\bullet\text{OH}$ ) [115]. These radical species efficiently participate in the oxidation of MB, leading to the formation of by-products such as carbon dioxide and water molecules, as elucidated in Scheme 2. The progression of this process is described by the following chemical reactions.

**Fig. 9** **A–F** **A** First cycle, **B** second cycle, **C** third cycle, and **D** fourth cycle replication of the UV-visible spectra. **E** Plot of degradation efficiency vs. number of cycles and **F** FT-IR spectra of ZnO/BC nanocomposite (a) before and (b) after four cycles for photocatalytic degradation of MB under sunlight irradiation





**Scheme 2** Photocatalytic degradation mechanism of MB with ZnO/BC composites under sunlight irradiation



## 4 Conclusion

This research employs a ZnO-coated biochar nanocomposite, synthesized from banana peels and zinc acetate dihydrate, to enhance the photocatalytic activity of the ZnO/BC nanocomposite. This approach is both cost-effective and environmentally friendly. The ZnO/BC nanocomposite boasts abundant active sites, facilitating a high adsorption capacity for MB and the generation of reactive radicals. Consequently, the photocatalytic degradation efficiency is significantly improved under sunlight irradiation.

The elimination of MB from wastewater using the ZnO/BC nanocomposite was modeled using the pseudo-first-order approach. An in-depth examination of the ZnO/BC nanocomposite's stability and reusability demonstrated consistent photocatalytic degradation efficiency (70%) for MB even after undergoing four cycles.

Scavenger studies further verified the participation of active radicals, including  $h^+$ ,  $e^-$ ,  $\cdot O_2^-$ , and  $\cdot OH$ , in the photocatalytic degradation of MB. Particularly, electron ( $e^-$ ) and hydroxyl ( $\cdot OH$ ) radicals played prominent roles in the degradation process under sunlight irradiation.

This ZnO/BC nanocomposite holds substantial potential for wide-scale implementation in wastewater treatment and environmental remediation endeavors.

**Supplementary Information** The online version contains supplementary material available at <https://doi.org/10.1007/s13399-024-05999-z>.

**Acknowledgements** We thank the University of Pretoria (Postdoctoral fellowship) for the financial support and the University of Johannesburg, Johannesburg, South Africa, for providing research facilities for this work. I am also thankful to Sri Paramakalyani College, Alwarukirichi (Department of Chemistry) providing laboratory facilities.

**Author contribution** Prabakaran Eswaran planned the project, data interpretation and wrote the first draft. Priya Dharshini Madasamy contributed to this work in the laboratory. Kriveshini Pillay contributed in visualization and study. Hendrik Brink contributed in supervision, writing, review, and editing.

**Funding** Open access funding provided by University of Pretoria. This work further received support from the Austrian Federal Ministry of Education, Science and Research (BMBWF) through Austria's Agency for Education and Internationalization (OeAD) [Grant Numbers: Africa UNINET P058 and APPEAR Project 341].

## Declarations

**Competing interests** The authors declare no competing interests.

**Open Access** This article is licensed under a Creative Commons Attribution 4.0 International License, which permits use, sharing, adaptation, distribution and reproduction in any medium or format, as long as you give appropriate credit to the original author(s) and the source, provide a link to the Creative Commons licence, and indicate if changes were made. The images or other third party material in this article are included in the article's Creative Commons licence, unless indicated otherwise in a credit line to the material. If material is not included in the article's Creative Commons licence and your intended use is not permitted by statutory regulation or exceeds the permitted use, you will need to obtain permission directly from the copyright holder. To view a copy of this licence, visit <http://creativecommons.org/licenses/by/4.0/>.

## References

- Manisalidis I, Stavropoulou E, Stavropoulos A, Bezirtzoglou E (2020) Environmental and health impacts of air pollution: a review. *Public Health Front* 8:505570
- Lavanya C, Rajesh Dhankar RD, Sunil Chhikara SC, Sarita Sheoran SS (2014) Degradation of toxic dyes: a review. *Int J Curr Microbiol App Sci* 3:189–199
- Mehdizadeh P, Orooji Y, Amiri O, Salavati-Niasari M, Moayedi H (2020) Green synthesis using cherry and orange juice and characterization of  $TbFeO_3$  ceramic nanostructures and their application as photocatalysts under UV light for removal of organic dyes in water. *Clean Prod* 252:119765
- Mustafa T, Sari A, Saleh TA (2018) Response surface optimization, kinetic and thermodynamic studies for effective removal of rhodamine B by magnetic AC/CeO<sub>2</sub> nanocomposite. *J Environ Manage* 206:170–177
- Bora LV, Mewada RK (2017) Visible/solar light active photocatalysts for organic effluent treatment: fundamentals, mechanisms and parametric review. *Renew Sustain Energy Rev* 76:1393–1421
- Tiwari JN, Mahesh K, Le NH, Kemp KC, Timilsina R, Tiwari RN, Kim KS (2013) Reduced graphene oxide-based hydrogels for the efficient capture of dye pollutants from aqueous solutions. *Carbon* 56:173–182
- Rashidi HR, Sulaiman MN, Hashim NA, Hassan CRC, Ramli MR (2015) Synthetic reactive dye wastewater treatment by using nano-membrane filtration. *Desalination and Water Treatment* 55(1):86–95
- Da Rosa ALD, Carissimi E, Dotto GL, Sander H, Feris LA (2018) Biosorption of rhodamine B dye from dyeing stones effluents using the green microalgae *Chlorella pyrenoidosa*. *J Clean Prod* 198:1302–1310
- Asghar A, Raman AAA, Daud WMAW (2015) Advanced oxidation processes for in-situ production of hydrogen peroxide/hydroxyl radical for textile wastewater treatment: a review. *J Clean Prod* 87:826–838
- Mollah MYA, Gomes JAG, Das KK, Cocke DL (2010) Electrochemical treatment of Orange II dye solution-use of aluminum sacrificial electrodes and floc characterization. *J Hazard Mater* 174:851–858
- Nguyen CH, Juang RS (2019) Efficient removal of cationic dyes from water by a combined adsorption-photocatalysis process using platinum-doped titanate nanomaterials. *J Taiwan Inst Chem Eng* 99:166–179
- Kyriakopoulos G, Xiarchos I, Doulia D (2006) Treatment of contaminated water with pesticides via adsorption. *Int J Environ Technol Manag* 6:515–524
- Li Y, Du Q, Liu T, Peng X, Wang J, Sun J, Wang Y, Wu S, Wang Z, Xia Y, Xia L (2013) Comparative study of methylene blue dye adsorption onto activated carbon, graphene oxide, and carbon nanotubes. *Chem Eng Res Des* 91:361–368
- Sahraei R, Pour ZS, Ghaemy M (2017) Novel magnetic bio-sorbent hydrogel beads based on modified gum tragacanth/graphene oxide: removal of heavy metals and dyes from water. *J Clean Prod* 142:2973–2984
- Iqbal T, Khan MA, Mahmood H (2018) Facile synthesis of ZnO nanosheets: structural, antibacterial and photocatalytic studies. *Mater Lett* 224:59–63
- Sirajudeen J, Nagaswarupa HP, Kumar MA, Kumar CR, Gurushantha K, Shekhar TS, Anantharaju KS, Mahesh KV, Sharma SC, Nagabhushana H (2017) Photocatalytic and Photoluminescence studies of ZnO nanomaterials by Banana peel powder. *Mater Today Proc* 4(11):11827–11836
- Peng Y, Ji J, Zhao X, Wan H, Chen D (2013) Preparation of ZnO nanopowder by a novel ultrasound assisted non-hydrolytic sol-gel process and its application in photocatalytic degradation of CI Acid Red 249. *Powder Technol* 233:325–330
- Yang Y, Pignatello JJ, Ma J, Mitch WA (2014) Comparison of halide impacts on the efficiency of contaminant degradation by sulfate and hydroxyl radical-based advanced oxidation processes (AOPs). *Environ Sci Tech* 48(4):2344–2351
- Yao Y, Wang L, Sun L, Zhu S, Huang Z, Mao Y, Lu W, Chen W (2013) Efficient removal of dyes using heterogeneous Fenton catalysts based on activated carbon fibers with enhanced activity. *Chem Eng Sci* 101:424–431
- Mousa HM, Alenezi JF, Mohamed IM, Yasin AS, Hashem AFM, Abdal-Hay A (2021) Synthesis of TiO<sub>2</sub>@ ZnO heterojunction for dye photodegradation and wastewater treatment. *J Alloys Compd* 886:161169
- Pellera FM, Giannis A, Kalderis D, Stegmann R, Wang JY, Gidaracos E (2012) Adsorption of Cu (II) ions from aqueous solutions on biochars prepared from agricultural by-products. *J Environ Manage* 96(1):35–42
- Leng L, Yuan X, Zeng G, Shao J, Chen X, Wu Z, Wang H, Peng X (2015) Surface characterization of rice husk bio-char produced by liquefaction and application for cationic dye (Machite green) adsorption. *Fuel* 155:77–85
- Dias D, Lapa N, Bernardo M, Godinho D, Fonseca I, Miranda M, Pinto F, Lemos F (2017) Properties of chars from the gasification and pyrolysis of rice waste streams towards their valorisation as adsorbent materials. *Waste Manag* 65:186–194
- Costa E, Sotelo JL, Calleja G, Marron C (1981) Adsorption of binary and ternary hydrocarbon gas mixtures on activated carbon: experimental determination and theoretical prediction of the ternary equilibrium data. *AIChE J* 27(1):5–12
- Aydoghmish SM, Hassanzadeh-Tabrizi SA, Saffar-Teluri A (2019) Facile synthesis and investigation of NiO–ZnO–Ag nanocomposites as efficient photocatalysts for degradation of methylene blue dye. *Ceram Int* 45(12):14934–14942
- Iervolino G, Zammit I, Vaiano V, Rizzo L (2020) Limitations and prospects for wastewater treatment by UV and visible-light-active heterogeneous photocatalysis: a critical review. *Heterogeneous Photocatalysis: Recent Advances*, (pp. 225–264). [https://doi.org/10.1007/978-3-030-49492-6\\_7](https://doi.org/10.1007/978-3-030-49492-6_7)
- Zou Q, Li H, Yang Y, Miao Y, Huo Y (2019) Bi<sub>2</sub>O<sub>3</sub>/TiO<sub>2</sub> photocatalytic film coated on floated glass balls for efficient removal of organic pollutant. *Appl Surf Sci* 467:354–360
- Ma R, Zhang S, Li L, Gu P, Wen T, Khan A, Li S, Li B, Wang S, Wang X (2019) Enhanced visible-light-induced photoactivity of type-II CeO<sub>2</sub>/g-C<sub>3</sub>N<sub>4</sub> nanosheet toward organic pollutants degradation. *ACS Sustain Chem Eng* 7(10):9699–9708
- Elango G, Roopan SM (2016) Efficacy of SnO<sub>2</sub> nanoparticles toward photocatalytic degradation of methylene blue dye. *J Photochem Photobiol B* 155:34–38
- Ivetic TB, Finčur NL, Đačanin LR, Abramović BF, Lukić-Petrović SR (2015) Ternary and coupled binary zinc tin oxide nanopowders: synthesis, characterization, and potential application in photocatalytic processes. *Mater Res Bull* 62:114–121
- Jiang D, Xue J, Wu L, Zhou W, Zhang Y, Li X (2017) Photocatalytic performance enhancement of CuO/Cu<sub>2</sub>O heterostructures for photodegradation of organic dyes: effects of CuO morphology. *Appl Catal B Environ* 211:199–204
- Abebe B, Murthy HCA, Amare E (2020) Enhancing the photocatalytic efficiency of ZnO: defects, heterojunction, and optimization. *Environ Nanotechnol Monit Manag* 14:100336
- Abdullah FH, Bakar NA, Bakar MA (2020) Low temperature biosynthesis of crystalline zinc oxide nanoparticles from *Musa acuminata* peel extract for visible-light degradation of methylene blue. *Optik* 206:164279
- Sánchez-Albores R, Cano FJ, Sebastian PJ, Reyes-Vallejo O (2022) Microwave-assisted biosynthesis of ZnO-GO particles

- using orange peel extract for photocatalytic degradation of methylene blue. *J Environ Chem Eng* 10(6):108924
35. Suresh R, Rajendran S, Kumar PS, Vo DVN, Cornejo-Ponce L (2021) Recent advancements of spinel ferrite based binary nanocomposite photocatalysts in wastewater treatment. *Chemosphere* 274:129734
  36. Tripathi M, Sahu JN, Ganesan P (2016) Effect of process parameters on production of biochar from biomass waste through pyrolysis: a review. *Renew Sustain Energy Rev* 55:467–481
  37. Dawood S, Sen TK, Phan C (2016) Adsorption removal of methylene blue (MB) dye from aqueous solution by bio-char prepared from Eucalyptus sheathiana bark: kinetic, equilibrium, mechanism, thermodynamic and process design. *Desalin Water Treat* 57(59):28964–28980
  38. Ahmadi S, Ganjidoust H (2021) Using banana peel waste to synthesize BPAC/ZnO nanocomposite for photocatalytic degradation of Acid Blue 25: influential parameters, mineralization, biodegradability studies. *J Environ Chem Eng* 9(5):106010
  39. Mohan D, Sarswat A, Ok YS, Pittman CU Jr (2014) Organic and inorganic contaminants removal from water with biochar, a renewable, low cost and sustainable adsorbent—a critical review. *Bioresour Technol* 160:191–202
  40. Alessandro AD, De Pergola G (2018) The Mediterranean diet: its definition and evaluation of a priori dietary indexes in primary cardiovascular prevention. *Int J Food Sci Nutr* 69(6):647–659
  41. Inyang M, Dickenson E (2015) The potential role of biochar in the removal of organic and microbial contaminants from potable and reuse water: a review. *Chemosphere* 134:232–240
  42. Nakarmi A, Bourdo SE, Ruhl L, Kanel S, Nadagouda M, Kumar Alla P, Pavel I, Viswanathan T (2020) Benign zinc oxide betaine-modified biochar nanocomposites for phosphate removal from aqueous solutions. *J Environ Manag* 272:111048
  43. Wang S, Zhou Y, Han S, Wang N, Yin W, Yin X, Gao B, Wang X, Wang J (2018) Carboxymethyl cellulose stabilized ZnO/biochar nanocomposites: enhanced adsorption and inhibited photocatalytic degradation of methylene blue. *Chemosphere* 197:20–25
  44. Iqbal MM, Imran M, Hussain T, Naeem MA, Al-Kahtani AA, Shah GM, Ahmad S, Farooq A, Rizwan M, Majeed A, Khan AR, Ali S (2021) Effective sequestration of Congo red dye with ZnO/cotton stalks biochar nanocomposite: modeling, reusability and stability. *J Saudi Chem Soc* 25:101176
  45. Akir S, Hamdi A, Addad A, Coffinier Y, Boukherroub R, Omrani AD (2017) Facile synthesis of carbon-ZnO nanocomposite with enhanced visible light photocatalytic performance. *Appl Surf Sci* 400:461–470
  46. Samadi M, Shivaee HA, Pourjavadi A, Moshfegh AZ (2013) Synergism of oxygen vacancy and carbonaceous species on enhanced photocatalytic activity of electrospun ZnO-carbon nanofibers: charge carrier scavengers mechanism. *App Catal A Gen* 466:153–160
  47. Gonçalves MG, da Silva Veiga PA, Fornari MR, Peralta-Zamora P, Mangrich AS, Silvestri S (2020) Relationship of the physicochemical properties of novel ZnO/biochar composites to their efficiencies in the degradation of sulfamethoxazole and methyl orange. *Sci Total Environ* 748:141381
  48. Yang C, Wang X, Ji Y, Ma T, Zhang Wang FY, Ci M, Chen D, Jiang A, Wang W (2019) Photocatalytic degradation of methylene blue with ZnO@C nanocomposites: kinetics, mechanism, and the inhibition effect on monoamine oxidase A and B. *NanoImpact* 15:100174
  49. Rahman QI, Ahmad M, Misra SK, Lohani M (2013) Effective photocatalytic degradation of rhodamine B dye by ZnO nanoparticles. *Mater Lett* 91:170–174
  50. Matos J (2016) Eco-friendly heterogeneous photocatalysis on biochar-based materials under solar irradiation. *Top Catal* 59(2):394–402
  51. Colmenares JC, Varma RS, Lisowski P (2016) Sustainable hybrid photocatalysts: titania immobilized on carbon materials derived from renewable and biodegradable resources. *Green Chem* 18(21):5736–50
  52. Luo Y, Zheng A, Xue M, Xie Y, Yu S, Yin Z, Xie C, Hong Z, Tan W, Zou W, Dong L (2022) Ball-milled Bi<sub>2</sub>MoO<sub>6</sub>/biochar composites for synergistic adsorption and photodegradation of methylene blue: kinetics and mechanisms. *Ind Crops Prod* 186:115229
  53. Leichtweis J, Silvestri S, Welter N, Vieira Y, Zaragoza-Sánchez PI, Chávez-Mejía AC (2021) Carissimi E. Wastewater containing emerging contaminants treated by residues from the brewing industry based on biochar as a new CuFe<sub>2</sub>O<sub>4</sub>/biochar photocatalyst. *Process Saf Environ Prot* 150:497–509
  54. Meena R, Abdullah M, Vasanthakumar V, Ravichandran D, Murugesan S (2024) Green biochar-supported ZnFe<sub>2</sub>O<sub>4</sub> composite photocatalyst derived from waste banana peel: a sustainable approach for highly efficient visible light-driven degradation of organic pollutants in wastewater. *Ionics* 28:1–2
  55. Kaur H (2023) Synergistic effect of biochar impregnated with ZnO nano-flowers for effective removal of organic pollutants from wastewater. *Appl Surf Sci Adv* 12:100339
  56. Kaur H, Roy T (2024) Sustainable removal of organic pollutants using biochar based ZnO composites: experimental and theoretical studies of remediation process. *Surf Interfaces* 49:104399
  57. Sun J, Lin X, Xie J, Zhang Y, Wang Q, Ying Z (2020) Facile synthesis of novel ternary g-C<sub>3</sub>N<sub>4</sub>/ferrite/biochar hybrid photocatalyst for efficient degradation of methylene blue under visible-light irradiation. *Colloids Surf A: Physicochem Eng Asp* 606:125556
  58. Saravanan R, Gupta VK, Narayanan V, Stephen A (2013) Comparative study on photocatalytic activity of ZnO prepared by different methods. *J Mol Liq* 181:33–41
  59. Weldegebrieal GK (2020) Synthesis method, antibacterial and photocatalytic activity of ZnO nanoparticles for azo dyes in wastewater treatment: a review. *Inorg Chem Commun* 120:108140
  60. Prabakaran E, Pillay K (2021) Self-assembled silver nanoparticles decorated on exfoliated graphitic carbon nitride/carbon sphere nanocomposites as a novel catalyst for catalytic reduction of Cr(VI) to Cr(III) from wastewater and reuse for photocatalytic applications. *ACS Omega* 6:35221–35243
  61. Bagheri S, Chandrappa KG, Hamid SBA (2013) Facile synthesis of nano-sized ZnO by direct precipitation method. *Der Pharma Chemica* 5(3):265–270
  62. Ahmad R, Hasan I (2017) Efficient remediation of an aquatic environment contaminated by Cr (VI) and 2, 4-dinitrophenol by XG-g-polyaniline@ZnO nanocomposite. *J Chem Eng Data* 62(5):1594–1607
  63. Pandey P, Kurchania R, Haque FZ (2015) Controlled hydrothermal synthesis, structural and optical analysis of nanometer-sized ZnO spheres. *Optik* 126(2):301–303
  64. Yogamalar NR, Bose AC (2011) Tuning the aspect ratio of hydrothermally grown ZnO by choice of precursor. *J Solid State Chem* 184(1):12–20
  65. Jafarirad S, Mehrabi M, Divband B, Kosari-Nasab M (2016) Bio-fabrication of zinc oxide nanoparticles using fruit extract of Rosa canina and their toxic potential against bacteria: a mechanistic approach. *Mater Sci Eng: C* 59:296–302
  66. Zheng QF, Wang YH, Sun YG, Niu HH, Zhou JR, Wang ZM, Zhao J (2014) Study on structural properties of biochar under different materials and carbonized by FTIR. *Spectrosc Spectr Anal* 34:962–966

67. Yu F, Tian F, Zou H, Ye Z, Peng C, Huang J, Zheng Y, Zhang Y, Yang Y, Wei X, Gao B (2021) ZnO/biochar nanocomposites via solvent free ball milling for enhanced adsorption and photocatalytic degradation of methylene blue. *J Hazard Mater* 415:125511
68. Lavand AB, Malghe YS (2015) Synthesis, characterization and visible light photocatalytic activity of nitrogen-doped zinc oxide nanospheres. *J. Asian Ceram Soc* 3(3):305–10
69. Liu J, Li E, You X, Hu C, Huang Q (2016) Adsorption of methylene blue on an agro-waste oil tea shell with and without fungal treatment. *Sci Rep* 6(1):38450
70. Luo J, Wu Y, Jiang M, Zhang A, Chen X, Zeng Y, Wang Y, Zhao Y, Wang G (2023) Novel ZnFe<sub>2</sub>O<sub>4</sub>/BC/ZnO photocatalyst for high-efficiency degradation of tetracycline under visible light irradiation. *Chemosphere* 311:137041
71. Lu J, Zhang Q, Wang J, Saito F, Uchida M (2006) Synthesis of N-doped ZnO by grinding and subsequent heating ZnO-urea mixture. *Powder Technol* 162(1):33–7
72. Han Q, Yang Y, Wang R, Zhang K, Liu N, Hong M (2021) Biochar derived from agricultural wastes as a means of facilitating the degradation of azo dyes by sulfides. *Catalysts* 11(4):434
73. Huff MD, Lee JW (2016) Biochar-surface oxygenation with hydrogen peroxide. *J Environ Manage* 165:17–21
74. Nahar A, Akbor MA, Shawon MT, Trisha SA, Akher US, Alam MA, Pinky NS, Alam MS, Afrose F, Hossain MS (2024) Biotite and ZnO embedded carbon aerogel composite for enhanced photocatalytic activity to degrade ciprofloxacin under sunlight stimulation. *Results Eng.* 102524. <https://doi.org/10.1016/j.rineng.2024.102524>
75. Kapoor RT, Rafatullah M, Siddiqui MR, Khan MA, Sillanpää M (2022) Removal of reactive black 5 dye by banana peel biochar and evaluation of its phytotoxicity on tomato. *Sustainability* 14(7):4176
76. Zhou N, Chen H, Xi J, Yao D, Zhou Z, Tian Y, Lu X (2017) Biochars with excellent Pb (II) adsorption property produced from fresh and dehydrated banana peels via hydrothermal carbonization. *Bioresour Technol* 232:204–210
77. Foroutan R, Mohammadi R, Ramavandi B, Bastanian M (2018) Removal characteristics of chromium by activated carbon/CoFe<sub>2</sub>O<sub>4</sub> magnetic composite and Phoenix dactylifera stone carbon. *Korean J Chem Eng* 35:2207–2219
78. Sun YT, Chen JD, Wei ZH, Chen YK, Shao CL, Zhou JF (2023) Copper ion removal from aqueous media using banana peel biochar/Fe<sub>3</sub>O<sub>4</sub>/branched polyethyleneimine. *Colloids Surf A: Physicochem Eng Asp* 658:130736
79. Le S, Jiang T, Li Y, Zhao Q, Li Y, Fang W, Gong M (2017) Highly efficient visible-light-driven mesoporous graphitic carbon nitride/ZnO nanocomposite photocatalysts. *Appl Catal B: Environ* 200:601–10
80. Tao S, Yang M, Chen H, Zhao S, Chen G (2018) Continuous synthesis of Ag/AgCl/ZnO composites using flow chemistry and photocatalytic application. *Ind Eng Chem Res* 57(9):3263–3273
81. Haase M, Weller H, Henglein A (1988) Photochemistry and radiation chemistry of colloidal semiconductors. 23. Electron storage on zinc oxide particles and size quantization. *J Phys Chem* 92(2):482–487
82. Smazna D, Rodrigues J, Shree S, Postica V, Neubüse G, Martins AF, Sedrine NB, Jena NK, Siebert L, Schütt F, Lupan O (2018) Buckminsterfullerene hybridized zinc oxide tetrapods: defects and charge transfer induced optical and electrical response. *Nanoscale* 10(21):10050–10062
83. Jing H, Ji L, Li Z, Wang Z, Li R, Ju K (2023) Zn/Fe bimetallic modified Spartina alterniflora-derived biochar heterostructure with superior catalytic performance for the degradation of malachite green. *Biochar* 5(1):29
84. He Y, Wang Y, Hu J, Wang K, Zhai Y, Chen Y, Duan Y, Wang Y, Zhang W (2021) Photocatalytic property correlated with microstructural evolution of the biochar/ZnO composites. *J Mater Res Technol* 11:1308–1321
85. Bai X, Wang L, Zong R, Lv Y, Sun Y, Zhu Y (2013) Performance enhancement of ZnO photocatalyst via synergic effect of surface oxygen defect and graphene hybridization. *Langmuir* 29:3097–3105
86. Son DI, Yang HY, Kim TW, Park WI (2013) Photoresponse mechanisms of ultraviolet photodetectors based on colloidal ZnO quantum dot-graphene nanocomposites. *Appl Phys Lett* 102:021105
87. Dhandapani KV, Anbumani D, Gandhi AD, Annamalai P, Muthuvenkatachalam BS, Kavitha P, Ranganathan B (2020) Green route for the synthesis of zinc oxide nanoparticles from Melia azedarach leaf extract and evaluation of their antioxidant and antibacterial activities. *Biocatal Agric Biotechnol* 24:101517
88. Li X, Sun P, Yang T, Zhao J, Wang Z, Wang W, Liu Y, Lu G, Du Y (2013) Template-free microwave-assisted synthesis of ZnO hollow microspheres and their application in gas sensing. *Cryst-EngComm* 15:2949–2955
89. Han J, Kwon JH, Lee JW, Lee JH, Roh KC (2017) An effective approach to preparing partially graphitic activated carbon derived from structurally separated pitch pine biomass. *Carbon* 118:431–437
90. Patel M, Kumar R, Pittman CU Jr, Mohan D (2021) Ciprofloxacin and acetaminophen sorption onto banana peel biochars: environmental and process parameter influences. *Environ Res* 201:111218
91. Van Thuan T, Quynh BT, Nguyen TD, Bach LG (2017) Response surface methodology approach for optimization of Cu<sup>2+</sup>, Ni<sup>2+</sup> and Pb<sup>2+</sup> adsorption using KOH-activated carbon from banana peel. *Surf Interfaces* 6:209–217
92. Lourenço MA, Zeng J, Jagdale P, Castellino M, Sacco A, Farkhondehfal MA, Pirri CF (2021) Biochar/zinc oxide composites as effective catalysts for electrochemical CO<sub>2</sub> reduction. *ACS Sustain Chem Eng* 9(15):5445–5453
93. Gonçalves NP, Lourenço MA, Baleuri SR, Bianco S, Jagdale P, Calza P (2022) Biochar waste-based ZnO materials as highly efficient photocatalysts for water treatment. *J Environ Chem Eng* 10(2):107256
94. Sabaa HM, El-Khatib KM, El-Kady MY, Mahmoud SA (2022) Spinel structure of activated carbon supported MFe<sub>2</sub>O<sub>4</sub> composites as an economic and efficient electrocatalyst for oxygen reduction reaction in neutral media. *J Solid State Electrochem* 26(12):2749–2763
95. Azzam AB, Tokhy YA, Dars FM, Younes AA (2023) Heterogeneous porous biochar-supported nano NiFe<sub>2</sub>O<sub>4</sub> for efficient removal of hazardous antibiotic from pharmaceutical wastewater. *Environ Sci Pollut Res* 30(56):119473–90
96. Hung MC, Yuan SY, Hung CC, Cheng CL, Ho HC, Ko TH (2014) Effectiveness of ZnO/carbon-based material as a catalyst for photodegradation of acrolein. *Carbon* 66:93e104
97. Chen M, Bao C, Hu D, Jin X, Huang Q (2019) Facile and low-cost fabrication of ZnO/biochar nanocomposites from jute fibers for efficient and stable photodegradation of methylene blue dye. *J Anal Appl Pyroly* 139:319–332
98. Edison TNJI, Atchudan R, Sethuraman MG, Lee Y R (2016) Reductive-degradation of carcinogenic azo dyes using *Anacardium occidentale* testa derived silver nanoparticles. *J Photochem Photobiol B: Bio* 162:604–610
99. Yu S, Zhou J, Ren Y, Yang Z, Zhong M, Feng X, Su B, Lei Z (2023) Excellent adsorptive-photocatalytic performance of zinc oxide and biomass derived N, O-contained biochar nanocomposites for dyes and antibiotic removal. *Chem Eng J* 451:138959

100. Prabakaran E, Pillay K (2019) Synthesis of N-doped ZnO nanoparticles with cabbage morphology as a catalyst for the efficient photocatalytic degradation of methylene blue under UV and visible light. *RSC Adv* 9:7509–7535
101. Salem IA, El-Maazawi MS (2000) Kinetics and mechanism of color removal of methylene blue with hydrogen peroxide catalyzed by some supported alumina surfaces. *Chemosphere* 41(8):1173–80
102. Wang C, Zhang Y, Yu L, Zhang Z, Sun H (2013) Oxidative degradation of azo dyes using tourmaline. *J Hazard Mater* 260:851–9
103. El-Bahy ZM, Ismail AA, Mohamed RM (2009) Enhancement of titania by doping rare earth for photodegradation of organic dye (Direct Blue). *J Hazard Mater* 166(1):138–43
104. Duan W, Wang N, Xiao W, Zhao Y, Zheng Y (2018) Ciprofloxacin adsorption onto different micro-structured tourmaline, halloysite and biotite. *J Mol Liq* 269:874–81
105. Sharma A, Dutta RK (2018) Se-doped CuO NPs/H<sub>2</sub>O<sub>2</sub>/UV as a highly efficient and sustainable photo-Fenton catalytic system for enhanced degradation of 4-bromophenol. *J Clean Prod* 185:464–75
106. Lou W, Kane A, Wolbert D, Rtimi S, Assadi AA (2017) Study of a photocatalytic process for removal of antibiotics from wastewater in a falling film photoreactor: scavenger study and process intensification feasibility. *Chem Eng Process: Process Intensification* 122:213–221
107. Patel K, Roondhe B, Dabhi SD, Jha PK (2018) A new flatland buddy as toxic gas scavenger: a first principles study. *J Hazard Mater* 351:337–345
108. Li J, Li Z, Yang Y, Kong B, Wang C (2018) Laboratory study on the inhibitory effect of free radical scavenger on coal spontaneous combustion. *Fuel Process Technol* 171:350–360
109. Rather GA, Nanda A, Pandit MA, Yahya S, Barabadi H, Saravanan M (2021) Biosynthesis of Zinc oxide nanoparticles using *Bergenia ciliate* aqueous extract and evaluation of their photocatalytic and antioxidant potential. *Inorg Chem Commun* 134:109020
110. Houas A, Lachheb H, Ksibi M, Elaloui E, Guillard C, Herrmann JM (2001) Photocatalytic degradation pathway of methylene blue in water. *Appl Catal B: Environ* 31(2):145–157
111. Prasad AR, Anagha M, Shamsheera K, Joseph A (2020) Biofabricated ZnO nanoparticles: direct sunlight-driven selective photodegradation, antibacterial activity, and thermoluminescence emission characteristics. *New J Chem* 44:8273–8279
112. Thi Luyen N, Van Nguyen K, Van Dang N, Quang Huy T, Hoai Linh P, Thanh Trung N, Nguyen VT, Thanh DV (2023) Facile one-step pyrolysis of ZnO/Biochar nanocomposite for highly efficient removal of methylene blue dye from aqueous solution. *ACS omega* 8(30):26816–26827
113. Wu Z, Zhong H, Yuan X, Wang H, Wang L, Chen X, Zeng G, Wu Y (2014) Adsorptive removal of methylene blue by rhamnolipid-functionalized graphene oxide from wastewater. *Water Res* 67:330–344
114. Cai K, Shen W, Ren B, He J, Wu S, Wang WA (2017) A phytic acid modified CoFe<sub>2</sub>O<sub>4</sub> magnetic adsorbent with controllable morphology, excellent selective adsorption for dyes and ultra-strong adsorption ability for metal ions. *Chem Eng J* 330:936–46
115. Li B, Wang Y (2013) Facile synthesis and enhanced photocatalytic performance of flowerlike ZnO hierarchical microstructures. *J Phys Chem C* 114:890–896

**Publisher's Note** Springer Nature remains neutral with regard to jurisdictional claims in published maps and institutional affiliations.